HHS Public Access

Author manuscript

Nat Struct Mol Biol. Author manuscript; available in PMC 2020 December 01.

Published in final edited form as:

Nat Struct Mol Biol. 2020 July ; 27(7): 625–634. doi:10.1038/s41594-020-0433-5.

Mechanism of ligand activation of a eukaryotic cyclic nucleotide-gated channel

Xiangdong Zheng[1,8], **Ziao Fu**[2,8], **Deyuan Su**[3,8], **Yuebin Zhang**[4], **Minghui Li**[1,7], **Yaping Pan**[5], **Huan Li**[1], **Shufang Li**[1,2], **Robert A. Grassucci**[2], **Zhenning Ren**[5], **Zhengshan Hu**[1], **Xueming Li**[6], **Ming Zhou**[5], **Guohui Li**[4], **Joachim Frank**[1,2], **Jian Yang**[1,3]

[1]Department of Biological Sciences, Columbia University, New York, NY 10027, USA

[2]Department of Biochemistry and Molecular Biophysics, Columbia University, New York, NY 10032, USA

[3]Key Laboratory of Animal Models and Human Disease Mechanisms of Chinese Academy of Sciences/Key Laboratory of Bioactive Peptides of Yunnan Province, Chinese Academy of Sciences, Kunming 650223, China

[4]State Key Laboratory of Molecular Reaction Dynamics, Dalian Institute of Chemical Physics, Chinese Academy of Sciences, Dalian 116023, China

[5]Department of Biochemistry and Molecular Biology, Baylor College of Medicine, Houston, TX 77030, USA

[6]Beijing Advanced Innovation Center for Structural Biology, Tsinghua-Peking Joint Center for Life Sciences, School of Life Sciences, Tsinghua University, Beijing 100084, China

[7]Current address: HIT Center for Life Sciences, School of Life Science and Technology, Harbin Institute of Technology, Harbin 150001, China

[8]These authors contributed equally to this work

Abstract

Cyclic nucleotide-gated (CNG) channels convert cyclic nucleotide binding and unbinding into electrical signals in sensory receptors and neurons. The molecular conformational changes underpinning ligand activation are largely undefined. We report both closed- and open-state atomic cryo-EM structures of a full-length *C. elegans* cGMP-activated channel TAX-4 reconstituted in

Correspondence should be addressed to J.Y. (jy160@columbia.edu), J.F. (jf2192@cumc.columbia.edu) or G.L. (ghli@dicp.ac.cn).

AUTHOR CONTRIBUTIONS

M.L. and J.Y. conceived and initiated the structural project, X.Z., Z.F., D.S., Y.Z., M.L., X.L., Y.P., M.Z., G.L., J.F. and J. Y. designed experiments, analyzed results, and wrote the manuscript. X.Z., D.S. and M.L. performed molecular biological and biochemical experiments. Z.F. and X.Z. performed and R.A.G. and S.L. assisted cryo-EM data acquisition and processing, X.Z. built the atomic models. G.L. designed molecular dynamics simulation (MDS) strategy, and G.L. and Y.Z. performed MDS. D.S. carried out and H.L. assisted HEK 293T cell recordings. M.Z. supervised and Y.P. performed liposome recordings and analysis, and Z.H. performed supplemental single-channel analysis. H.L. performed confocal imaging and Z.R. performed liposome flux assays (data not shown). All authors contributed to manuscript discussion, preparation and editing.

COMPETING INTERESTS

The authors declare no competing interests.

lipid nanodiscs. These structures, together with computational and functional analyses and a mutant channel structure, reveal a double-barrier hydrophobic gate formed by two S6 amino acids in the central cavity. cGMP binding produces global conformational changes that open the cavity gate located ~52 Å away but do not alter the structure of the selectivity filter – the commonly presumed activation gate. Our work provides mechanistic insights into the allosteric gating and regulation of cyclic nucleotide-gated and -modulated channels and CNG channel-related channelopathies.

Cyclic nucleotide-modulated ion channels are present in prokaryotes and eukaryotes and play important physiological functions [1–3]. In eukaryotes, they are grouped into cyclic nucleotide-gated (CNG) channels and hyperpolarization-activated cyclic nucleotide-modulated (HCN) channels. CNG channels are essential for smell and vision in vertebrates. In olfactory receptors and photoreceptors, CNG channels open and close (i.e., gate) in response to stimuli-induced changes in the intracellular concentrations of cyclic adenosine monophosphate (cAMP) or cyclic guanosine monophosphate (cGMP), thereby transducing biochemical signals into electrical and calcium signals [1–3]. CNG channels are also expressed in the central nervous system where they modulate neuronal and glial functions [1,3]. Numerous hereditary mutations in CNG channel genes have been associated with degenerative visual disorders such as retinitis and achromatopsia, for which new treatment strategies are being explored [1,3,4].

CNG channels are nonselective cation channels [1–3,5–9]. They are formed by four subunits, each containing six transmembrane (TM) segments (S1-S6) and a pore-loop between S5 and S6 [1–3]. Although CNG channels belong to the voltage-gated ion channel (VGIC) superfamily and have an S4 decorated with multiple positively charged amino acids [1–3,7,8], they are not activated by TM voltage owing to the unique structure of S4 and its interactions with other regions [10]. CNG channels are activated by intracellular cAMP or cGMP, which bind to a cyclic nucleotide-binding domain (CNBD) in the intracellular C-terminus [1–3,7,8]. A ~80-amino acid linker (called the C-linker) connecting the CNBD and S6 is crucial for ligand activation [11–16]. Functional studies suggest that CNG channels have a single activation gate located in the ion selectivity filter (SF) [17–21], a view that has been widely accepted [3,10,22,23] but has also been challenged [24].

Despite extensive functional and structural studies, the way cyclic nucleotides (CN) activate CNG channels and whether the SF is in fact the activation gate remains largely unclear. This paucity of knowledge is due in part to a lack of structures of a full-length CNG channel in both the unliganded closed-state and liganded open-state. Work on prokaryotic CN-modulated channels such as MloK1, LliK and SthK has produced only closed-state structures, even in cases where a CN is bound to the CNBD [25–27]. We recently reported a liganded open-state cryo-EM structure of a eukaryotic CNG channel TAX-4 [10], a cGMP-activated channel in *Caenorhabditis elegans* [16,28,29]. In this study we determined single-particle cryo-EM structures of full-length TAX-4 reconstituted in lipid nanodiscs in a cGMP-unbound closed state and a cGMP-bound open state at 2.6 Å and 2.7 Å resolutions, respectively. We also carried out computational analyses and structure-guided mutagenesis to elucidate the ion permeation pathway. Our work reveals a single double-barrier

hydrophobic gate in the central cavity and a conformational trajectory from the CNBD to the cavity gate in association with channel gating.

RESULTS

cGMP-unbound and cGMP-bound structures

To obtain a cGMP-unbound structure, full-length TAX-4 was purified in the presence of 100 μM cGMP as previously described [10], but cGMP was omitted in the final gel filtration elution buffer. The purified apo protein formed cGMP-activated channels when reconstituted in liposomes (Fig. 1a). For single-particle cryo-EM analysis, the protein was reconstituted in lipid nanodiscs (Extended Data Fig. 1). A cryo-EM density map of unliganded TAX-4 tetramer was obtained at an overall resolution of 2.6 Å and 2.8 Å with imposed *C4* and *C1* symmetry, respectively (Fig. 1b, Extended Data Figs. 1 and 2, and Table 1). The local resolution varies from 2.4 Å in some TM and cytoplasmic regions to 3.0 Å in the peripheries of the 3D reconstruction with *C4* symmetry (Extended Data Fig. 1h). The densities were of excellent quality for most functional regions (Extended Data Fig. 2). We were able to model 513 of the 733 amino acids of TAX-4 in the final structure (Table 1). Residues M1 to V103 (N-terminus), G162 to L164, and D620 to K733 (distal C-terminus) were not modeled because of weak or missing densities.

The previous cGMP-bound open-state TAX-4 structure was obtained in amphipol [10]. To ensure adequate comparison with the cGMP-unbound structure, we determined the cryo-EM structure of cGMP-bound TAX-4 in lipid nanodiscs (Extended Data Fig. 3 and Table 1). The overall resolution reached 2.7 Å and 2.9 Å with imposed *C4* and *C1* symmetry, respectively, which is significantly higher than the 3.5 Å-resolution in amphipol. The cGMP-bound structures in nanodiscs and amphipol are highly similar, with an α-carbon r.m.s.d of 0.9 Å when all of the 512 resolved amino acids are superimposed.

The overall architecture of cGMP-unbound TAX-4 is similar to that of cGMP-bound TAX-4 (Fig. 1c,d). The channel is a tetramer and has a non-domain swapped configuration (Fig. 1c). As described previously [10], each protomer can be arbitrarily divided into four structural layers along the fourfold axis: an extracellular domain comprising mainly of the S1-S2 linker, a transmembrane domain (TMD) comprising of S1-S6 and the pore-loop, a gating ring formed by helices A'B'C'D' of the C-linker, which also contains helices E'F', and the CNBD (Fig. 1d).

As the primary goal of this work is to determine cGMP-induced conformational changes in the full-length channel, and since it is unknown *a priori* which regions of TAX-4 remain static during cGMP activation, we opted to superimpose the cGMP-unbound and -bound structures based on an alignment of all resolved atoms (see METHODS for details). The global and local structural comparisons described below are all based on this alignment. Global comparison reveals marked conformational changes in many parts of the channel (Fig. 1d and Supplementary Video 1), as detailed below. The α-carbon and all-atom r.m.s.d of global superposition is 2.6 Å and 3.0 Å, respectively. The entire channel contracts by ~5.9 Å upon cGMP binding to the CNBD. Contraction is most dramatic in the CNBD and C-linker (Fig. 1d and Supplementary Video 1).

A hydrophobic gate in the central cavity

The ion conduction pore traverses all four structural layers. In the cGMP-bound structure, the pore has a single constriction at E379 of the SF, and the inner pore formed by S6 is wide open (Fig. 2b,c). In striking contrast, the pore of the cGMP-unbound structure has three constrictions, one at E379, one at F403 of S6, and one at V407 of S6 (Fig. 2a,c). The side-chains of F403 and V407 point away from the pore axis in the cGMP-bound structure (Figs. 2b and 3a) but protrude into the pore lumen in the cGMP-unbound structure (Figs. 2a and 3a). As a consequence, the pore narrows dramatically at F403 and V407, from a diameter of 23.1 Å and 14.6 Å in the cGMP-bound structure to 5.9 Å and 5.7 Å in the cGMP-unbound structure, respectively (Fig. 3a). Computational analyses based on the recently developed Channel Annotation Package (CHAP) [30,31] indicate that the side-chains of F403 and V407 pose a prohibitive high-energy barrier for water molecules in the cGMP-unbound structure and that water molecules readily permeate the pore region at F403 and V407 in the cGMP-bound structure but are repelled from this region in the cGMP-unbound structure (Fig. 2d). Since water permeability serves well as a proxy for ion permeability [30–32], the side-chains of F403 and V407 most likely form a hydrophobic gate that prevents the flow of hydrated and partially hydrated Na^+, K^+ and Ca^{2+} ions. These structures and analyses suggest that the cGMP-unbound and -bound structures represent closed state and open state, respectively, and that F403 and V407 form a double-barrier hydrophobic gate.

F403 is located in the middle of the membrane and immediately below the SF, and V407 is one α-helical turn down (Fig. 3). These positions correspond to the aqueous central cavity in many VGICs) [33,34]. Thus, we referred to the F403-V407 hydrophobic gate as cavity gate.

Most VGICs have an inner gate at the cytoplasmic end of S6. The narrowest inner pore diameter of TAX-4 in the closed state is 9.1 Å at S415 (see Fig. 1d for its position). Thus, although the TAX-4 inner pore narrows markedly upon cGMP unbinding (Fig. 2a–c), it is sufficiently wide to permit conduction of hydrated Na^+, K^+ and Ca^{2+} ions. S415 corresponds to or is close to amino acids that form the inner gate in many channels, including TRPV1 and HCN1 [34,35]. Thus, TAX-4 does not appear to have an inner gate.

No conformational change at the selectivity filter

Currently, it is generally accepted that the activation gate of CNG channels is located in the SF [3,10,22,23], despite some contention [24]. This view is based on state-dependent block and cysteine modification of CNG channel pores by Ag^+, Cd^{2+} or methanethiosulfonate compounds [17–21,36]. However, our structures show that the SF is virtually identical in the closed and open states (Fig. 3a), thus challenge this prevailing view. The TAX-4 SF is formed by the side-chains and backbone carbonyl oxygens of four conserved amino acids, T376, I377, G378 and E379 (Fig. 3a,b). Paradoxically, the narrowest constriction along the ion conduction pathway in both the closed and open states is formed by the side-chains of E379 at the external entrance of the SF (Figs. 2a–c and 3a). This constriction has a similar size in the closed and open states, measuring 4.2 Å and 4.6 Å in diameter, respectively (Fig. 3a). It is the narrowest constriction in the pore because the carboxylates of E379 extend to the center to provide dehydration and salvation to the permeating cations. CHAP analyses show the highest water density at the E379 constriction in both open and closed states (Fig.

2d), suggesting that Na^+, K^+ or Ca^{2+} ions can readily permeate this constriction in both states. The rest of the SF is >7.5 Å in diameter in both closed and open states (Fig. 3a) and permits water permeation (Fig. 2d). These structures and analyses indicate that cGMP binding does not significantly change the structure of the SF under our experimental conditions.

The densities of E379 side-chains are strong and unambiguous in both open and closed states (Fig. 3b,c) and show that E379 does not interact with any other amino acids in either state. A weak density is observed at the center of the SF between the carbonyl oxygen rings of T376 and I377 in the open state (Fig. 3c). This density also appears in the *C1* reconstruction (data not shown) but does not appear in half maps (Extended Data Fig. 3i). It is thus uncertain whether this density represents an ion or is an artifact. On the other hand, a robust density is observed at the center of E379 side-chains in the closed state (Fig. 3b). This density is also present in the *C1* reconstruction (data not shown) and half maps (Extended Data Fig. 1i) and therefore most likely represents a bound ion. Since Na^+ and contaminating Ca^{2+} are the only cations in the protein sample, the observed density likely represents a bound Na^+ or Ca^{2+} ion. The precise nature and identity of this density awaits future elucidation.

Functional and structural examination of the cavity gate

If F403 and V407 form the sole activation gate, one would expect that a mutant TAX-4 channel without such a gate would conduct basal currents in the absence of cGMP. To test this hypothesis, we created F403A, V407A and F403A-V407A mutant channels and recorded their currents in HEK 293T cells. The wild-type (WT) channel had no basal currents but produced large cGMP-activated currents (Fig. 4a,b). F403A and V407A also had no basal current (Fig. 4b), which is expected since the other hydrophobic barrier is still intact and the cavity gate is therefore still closed. However, F403A-V407A had no basal current, and strikingly, none of the single or double alanine mutant channels had cGMP-activated currents (Fig. 4b), even though the channels were expressed on the plasma membrane (data not shown). Inspection of the closed- and open-state structures shows that F403 and V407 are engaged in extensive van der Waals interactions with other amino acids in both states (see later). Disrupting these interactions likely destabilizes both states. The detrimental effect of the F403A-V407A mutation suggests that mutating F403 and V407 together to glycine or polar amino acids would also destabilize both closed and open states and that any attempt to obtain a constitutively open TAX-4 channel by simultaneously mutating these amino acids would be difficult.

In some channels, hydrophobic gates form at locations where the pore is physically wide enough to accommodate partially or even fully hydrated Na^+ or K^+ ions [30,31]. The pore of TAX-4 is 5.9 and 5.7 Å wide at F403 and V407, respectively, in the closed state (Fig. 3a). To examine the robustness of the F403-V407 hydrophobic gate, we created F403V-V407A, reasoning that a valine at position 403 may maintain some of the van der Waals interactions but, with the much smaller valine and alanine at positions 403 and 407, the pore would be significantly wider in the absence of cGMP. The F403V-V407A mutant channel (named VA) showed no cGMP-induced currents when expressed in HEK 293T cells (Fig. 4b) and

displayed sporadic cGMP-evoked currents in only 2 out of 20 single-channel recordings when reconstituted in liposomes (Fig. 4c), indicating an impaired activation by cGMP. This is expected since the V407A mutation alone impaired activation by cGMP (Fig. 4b). Interestingly, F403V-V407A exhibited a small but significant increase in outward basal current (Fig. 4a). There was no increase in inward basal current; the reason for this is unclear but could be asymmetric ion block and/or ion permeation in the mutant channel pore. The outward basal current is unlikely produced by voltage-dependent activation of the mutant channel, because WT TAX-4 does not respond to voltage (Fig. 4a) [10] and because the structure of S4 and other parts of the voltage sensor-like domain is unaltered by the F403V-V407A double mutation (Fig. 4d). The outward basal current is also unlikely to be caused by spontaneous openings of the mutant channel, which showed no activity in the absence of cGMP in 20 out of 20 liposome recordings. A parsimonious explanation for the small basal current is that the cavity gate becomes slightly leaky in F403V-V407A, and the resulting leak current is too miniscule to be detected by single-channel recording (Fig. 4c) but the macroscopic leak current is measurable by whole-cell recording (Fig. 4a).

To test this hypothesis and understand why F403V-V407A has but a small basal current, we solved its structure in a cGMP-unbound state (Extended Data Fig. 4 and Table 1). The mutant structure, determined at a 2.5 Å-resolution, is virtually identical to the WT closed-state structure (Fig. 4d), with an α carbon r.m.s.d of 0.5 Å when all of the 513 resolved amino acids are superimposed. The side-chains of V403 and A407 point to the cavity (Fig. 4e,h), as the side-chains of F403 and V407 do in WT closed state. As expected, the pore widens significantly at these positions when compared to WT closed state (Fig. 4f,h). CHAP analyses indicate that although V403 still poses a high energy barrier, water permeation is not completely absent in the mutant pore as in the WT pore (Fig. 4g). This structure is thus in good agreement with the small basal current observed in the mutant channel (Fig. 4a). These functional and structural results support the hypothesis that V407 and A403 still form a hydrophobic gate in the F403V-V407A mutant channel, but this gate is slightly leaky. They also reinforce the conclusion that F403 and V407 form a strong double-barrier hydrophobic gate in the WT channel.

CNBD and C-linker conformational changes

The cGMP-binding site is ~51-54 Å from the cavity gate. The conformational changes triggered by cGMP binding are essentially propagated from the CNBD to the cavity gate through the C-linker (Fig. 1c,d). The overall structure of the TAX-4 CNBD is similar to that of other CN-binding proteins [26,27,35,37–43] and is composed of four α helices (designated A, B, C and P) and a β-roll containing eight β sheets (Fig. 5a,b). cGMP binding causes most parts of the CNBD to contract, bringing the α helices and β-roll closer together to cradle a cGMP molecule in a conserved binding pocket (Fig. 5a,b and Supplementary Video 1). The C-helix undergoes the largest movement upon cGMP binding: it rotates counterclockwise with respect to the TMD by 17.5^{o} when viewed from the intracellular side (Fig. 5c) (same view below unless noted otherwise) and moves vertically towards cGMP and the TMD by > 2.9 Å (Fig. 5d). Helices A, B and P and the β-roll also move toward cGMP. These movements cause the C-linker to undergo dramatic and complex conformation rearrangements (Figs. 5, 6 and Supplementary Video 1). The C-linker is composed of α

helices A'-F', of which A'B'C'D' form the gating ring. Helices A'B' of one subunit associate with helices C'D' and S4-S5-S6 of the counterclockwise neighboring subunit in both closed and open states. Upon cGMP binding, helices E' and F' move vertically toward the TMD by 7.1 Å and 6.6 Å, respectively (Fig. 5e). This large upward movement causes the gating ring to move closer to the TMD and to tilt. Helices C' and D' move up vertically by 3.2 Å and 3.3 Å, respectively (Fig. 5e). Helix A' rotates counterclockwise by 2° (Fig. 6a), tilts towards the center by 15° (Fig. 6b), and moves up vertically by 1.1-5.9 Å (Fig. 6c). These movements increase the distance between two diagonally opposed A419 from 17.9 Å to 24.7 Å (Fig. 6a); A419 is located at the N-terminal end of helix A' and connects with S6 (for location, see Fig. 1d).

S6 conformational changes

S6 interacts strongly with S5 and pore-helix of the same subunit and S6 of the counterclockwise neighboring subunit (Fig. 7a,b). The interactions are mostly different in the closed and open states. Notably, F403 and V407 form extensively van der Waals contacts in both the closed and open states (Fig. 7b). These residues thus play a dual role: forming a hydrophobic cavity gate and stabilizing the closed and open states.

Previous cysteine mutagenesis and modification studies suggest that S6 undergoes rotational and translational motions during ligand gating of CNG channels [17,36]. Our TAX-4 structures show that the cGMP binding-induced movement of the gating ring causes a movement of most parts of the TMD, with the largest movement in S5 and S6 (Supplementary Videos 1 and 2). S6 connects to the gating ring via a 2-amino acid (M417 and S418) linker (Fig. 1d and Supplementary Figure 1). Inserting a single glycine between M417 and S418 disrupts cGMP activation of TAX-4 [10], indicating that a direct connection between S6 and the gating ring is crucial for ligand activation. This connection takes place between N416 of S6 and A419 of helix A' (Fig. 1d and Supplementary Figure 1). The radial expansion of A419 from the central axis upon cGMP binding pulls on the intracellular end of S6, and this pulling, together with the movements of other TMD regions, leads to a dilation of the inner pore (from 9.1 Å to 18.0 Å at S415) and a right-handed twist of S6 (Fig. 7c). The degree of this twist varies at different positions, with the largest twist at F403 and V407 (4.2° at G399, 43.8° at F403, 51.8° at V407, and 18.2° at S415). Due to this twist, the side-chains of F403 and V407 undergo a 98° and 51° clockwise rotation (Fig. 7d,e and Supplementary Video 2). It is this rotation that opens the cavity gate. The main hinge point for S6 twisting and splaying is G399 (for location, see Fig. 1d). This glycine is conserved from prokaryotic CN-modulated channels to human CNG channels, as is the cavity gate (Supplementary Figure 1), suggesting that the cGMP binding-induced S6 conformational changes described for TAX-4 is a conserved gating mechanism.

DISCUSSION

The high-resolution structures of TAX-4 illuminate several new aspects of CNG channel gating, provide an alternative explanation for some previous results, and raise questions on some earlier conclusions. First, a spatial conformational trajectory of allosteric gating by cGMP is revealed. The conformational changes are complex (Supplementary Video 1) but

can be simplified into four steps. (1) cGMP binding causes the CNBD to contract, with its α helices and β-roll approaching the bound ligand. (2) The CNBD-contacting E'F' helices of the C-linker move up toward the membrane. (3) Helix A' of the gating ring tilts, rotates counterclockwise, and moves toward the membrane, causing its S6-connecting end to expand drastically. (4) S6 dilates and twists, and as a result, the side-chains of F403 and V407 swing away from the pore axis (Fig. 7b–e and Supplementary Videos 1 and 2).

Local structural comparisons of isolated apo and liganded CNBDs have revealed some of the CN-induced movements observed in the full-length TAX-4 structures, especially the large movement of the C-helix [26,27,37–43]. The CNBDs of full-length MloK1 and SthK move toward the membrane by A 3-6 Å [44,45]. Moreover, the CNBDs of LliK and SthK splay apart radially by 4 Å or more [26,45], and the CNBD of SthK rotates 25º clockwise with respect to the TMD [45]. In contrast, although the C helix moves toward the membrane and undergoes a significant counterclockwise rotation, the CNBD of TAX-4 as a whole does not move vertically toward the membrane or splay apart upon cGMP binding (Supplementary Video 1). The reasons for and importance of these differences await elucidation.

HCN channels are modulated by CNs and contain a CNBD and C-linker. Structures of apo and cAMP-bound full-length human HCN1 have been determined [35]. Superposition of the C-linkers and CNBDs of HCN1 and TAX-4 based on an alignment of the β-roll shows that although the overall structures of these regions are similar in the two channels, significant local differences exist in both apo and liganded states (Extended Data Fig. 5). In particular, the CN-induced conformational changes of helix A' of the C-linker are much smaller in HCN1 than in TAX-4. Thus, the displacement of S6 is much smaller in HCN1 than in TAX-4, consistent with the fact that HCN1 is not activated by CNs in the absence of hyperpolarization.

Second, CNs open a hydrophobic gate in the central cavity. VGICs are known to have two gates, one located at the intracellular end of the S6 bundle (the inner gate), one in the SF (the SF gate) [46]. Some channels have both gates (e.g., Kv channels and TRPV1[34,46]) and some have only the inner gate (e.g., TRPML3[47]). Our work demonstrates the existence of a third gate − a gate in the central cavity. The presence of this hydrophobic cavity gate explains some of the unique pharmacological properties of CNG channels, such as the profound closed-state block by the local anesthetic tetracaine [48,49]. A hydrophobic cavity gate is also observed in the closed-state structures of bacterial CN-modulated channels, and is formed by Y224 and I228 in LliK, F203 in MloK1, and Y211 and I215 in SthK [25–27] (Supplementary Figure 1 and Extended Data Fig. 6). Although a number of ion channels have hydrophobic gates [30,31], no other VGIC has been reported to possess a hydrophobic gate in the central cavity. Thus, it appears that the hydrophobic cavity gate is a unique structural feature evolved in bacterial CN-modulated channels and preserved in eukaryotic CNG channels.

The lack of an inner gate in TAX-4 explains previous cysteine modification data from vertebrate CNG channels showing that some positions above the S6 bundle crossing were readily accessible to intracellular thiol-modifying reagents when the channels were closed [17–21,36]. Those observations were originally interpreted in the context of the KcsA structure [33] and led to the hypothesis that the CNG channel activation gate was located not at the S6

bundle crossing but at the SF. A key observation that led to the SF gate proposition was the state-dependent modification by intracellular Ag^+ of cysteine residues engineered at the SF [19]. In this study, cysteines at the equivalent positions of T376 and I377 (for position, see Fig. 3) were modified by Ag^+ in open and closed states with similar rates (between 10^6-10^7 $M^{-1}S^{-1}$); on the other hand, a cysteine at the equivalent position of V380 was modified 200 times more slowly in the closed state (10^4 $M^{-1}S^{-1}$) than in the open state (2×10^6 $M^{-1}S^{-1}$). An activation gate was proposed to be formed by the backbone movement of a glycine equivalent to G378 [19]. However, it is unclear based on the TAX-4 structures how Ag^+ modification of a cysteine at the equivalent position of V308 would inhibit the channel. Moreover, the TAX-4 structures show that G378 moves little upon cGMP binding and unbinding (Fig. 3a). Whether the SF of vertebrate and native CNG channels has a structure different from that of TAX-4 and whether it undergoes CN-induced movements and forms an activation gate remains to be determined.

Third, the closed and open states are stabilized by numerous and distinct interactions between many regions. The interaction interfaces vary among different CNG channel subunits (Supplementary Figure 1), explaining in part the different affinities and efficacies of CN activation of different CNG channels [1,3]. Altering the strength of these interactions would be expected to affect CNG channel gating, as has been observed in cases where some of the interactions are disrupted or strengthened [11–16,36,50–52].

Fourth, although the SF does not change its conformation upon cGMP binding and unbinding, it may nevertheless play a role in gating. Notably, the side-chains of E379 do not interact with any other amino acids in either the closed or open state; instead, they appear to interact with a cation in the closed state but not in the open state (Fig. 3b, c). This interaction may stabilize the closed state. The effects of E379 mutations on CNG channel gating [53,54] thus need to be reinterpreted in light of these structural observations.

Finally, CNG channels are modulated by various membrane lipids [55–61]. Discrete and strong densities not belonging to the channel protein are observed in both cGMP-unbound and -bound structures (Extended Data Fig. 7). These densities may represent lipids. Indeed, some densities can be modeled as specific lipid molecules (Extended Data Fig. 7). The functional importance of lipid binding to TAX-4 awaits further investigation.

METHODS

Molecular biology.

Cloning of the TAX-4 coding sequence into various expression vectors was conducted as described previously [10]. Briefly, the full-length TAX-4 gene was amplified from a *Caenorhabditis elegans* cDNA library by PCR. The WT TAX-4 gene was cloned into a modified pFastBac1 vector for expression of MBP-tagged full-length TAX-4 protein, and into the pcDNA3.1(−) vector (Invitrogen) for electrophysiology experiments. All TAX-4 mutants used in protein purification and electrophysiology experiments were created using the Q5® Site-Directed Mutagenesis Kit (New England Biolabs) and were verified by sequencing. For surface expression experiments, a construct named GFP-TAX-4_WT-HA was created as described previously [10]. Briefly, the full-length WT TAX-4 gene was cloned

into a modified pEGFP_C1 vector, generating a construct called GFP-TAX-4_WT. Then, a sequence of GGGYPYDVPDYAGGG, which contains the hemagglutinin (HA) tag (underlined) and flanking sequences, was inserted between G162 and T163 in GFP-TAX-4_WT. The resulting GFP-TAX-4_WT-HA channel thus contains a GFP tag on its N-terminus and an HA tag in the extracellular linker between S1 and S2. All site-specific mutants were subsequently generated in TAX-4_WT and GFP-TAX-4_WT-HA by PCR-based overlapping extension mutagenesis.

Protein expression, purification and nanodisc reconstitution.

The baculovirus of WT and mutant TAX-4 was generated with Sf9 cells (Invitrogen, not tested for mycoplasma) following the standard protocol and used to infect Sf9 cells for protein expression at a ratio of 1:50 (virus to Sf9, v/v). Forty-eight hours after infection, cells were harvested by centrifugation at 4,539 g. All purification procedures were carried out at 4 °C unless specified otherwise. The cell pellet was re-suspended and lysed by osmotic shock in a hypotonic buffer (20 mM Tris-Cl, pH 8.0, 5 mM β-mercaptoethanol, 100 μM cGMP) supplemented with a protease inhibitor cocktail (Sigma). After lysis, cell membranes were collected by centrifugation at 29,448 g for 30 min. TAX-4 protein was further extracted from cell membranes using a glass dounce homogenizer in an extraction buffer (50 mM HEPES-Na, pH 8.58, 150 mM NaCl, 0.5% LMNG, 5 mM β-mercaptoethanol, 100 μM cGMP). After incubation for 1 h, the solubilized membrane was clarified by ultracentrifugation at 111,338 g for 30 min and incubated with amylose resin (New England Biolabs) for 2 h with gentle agitation. The resin was collected by low speed spin at 800 *g*, transferred into a gravity column, and washed with buffer A (50 mM HEPES-Na, pH 8.58, 150 mM NaCl, 0.05% LMNG, 0.15 mM soybean polar lipid extract (Avanti), 5 mM β-mercaptoethanol, 100 μM cGMP) and subsequently buffer B (50 mM HEPES-Na, pH 7.4, 500 mM NaCl, 0.05% LMNG, 0.15 mM soybean polar lipid extract, 5 mM β-mercaptoethanol, 100 μM cGMP). Maltose (20 mM) in the wash buffer B was used to elute the MBP-tagged TAX-4 protein. The eluted MBP-tagged TAX-4 protein was concentrated to 1 ml before nanodisc reconstitution.

Membrane scaffold protein MSP2N2 was expressed and purified from *Escherichia coli*, and MBP-tagged TAX-4 protein was incorporated into lipid nanodiscs following the published protocol [62]. In brief, MBP-TAX-4, MSP2N2 and soybean polar lipids (dissolved in a buffer containing 50 mM HEPES-Na, pH 7.4, 500 mM NaCl, 33 mM CHAPS) were mixed at a molar ratio of 1:2.5:200, and incubated on ice for 20 min. Bio-beads SM2 (200 mg per 1 ml mixture, Bio-Rad) were added to initiate the reconstitution by removing detergents from the system and the mixture was incubated at 4 °C with gentle agitation for 1 h. A second batch of Bio-beads (same amount as above) together with TEV protease (100 μg per 1 mg MBP-TAX-4) was then added and the sample was incubated at 4 °C overnight. The TAX-4/nanodisc sample was centrifuged to remove Bio-beads and concentrated to 0.5 ml before the final separation with a Superose 6 column (GE). The elution peak corresponding to reconstituted TAX-4/nanodisc was collected for cryo-EM analysis. For cGMP-bound WT TAX-4/nanodisc sample, the protein was eluted with a gel-filtration buffer containing 50 mM HEPES-Na, 500 mM NaCl, 5 mM β-mercaptoethanol, pH 7.4, with 100 μM cGMP. For

cGMP-unbound WT and F403V-V407A mutant TAX-4/nanodisc samples, the proteins were eluted with the same buffer but without cGMP.

Cryo-EM sample preparation and data acquisition.

The cryo-EM grids were prepared by applying 3 μl of TAX-4/nanodisc sample (0.75 mg ml $^{-1}$ with or without the addition of 2 mM cGMP) to a glow-discharged UltrAuFoil holey gold R0.6/1 grid (Quantifoil Micro Tools). After waiting for 30 s, the grid was blotted for 8 s (double-sided, blot force 3) under 100% humidity and 4 °C using FEI Vitrobot Mark IV (FEI) and immediately plunged into liquid mixture of ethane and propane 37%:63% cooled by liquid nitrogen. Micrographs were acquired by a FEI Titan Krios microscope (Thermo Fisher) operated at 300 kV and equipped with a K2 Summit direct electron detector (Gatan) working at counting mode. Leginon [63] was used for data collection. A nominal magnification of 22,500 × was used for imaging the samples, corresponding to a final pixel size of 1.07 Å on image. The defocus ranged from −1.5 μm to −3 μm. Each micrograph was dose-fractionated to 47 movie frames under a dose rate of 8.09 counts per pixel per second, with a total exposure time of 9.4 s and a frame exposure time of 0.2 s, resulting in a total dose of 66.03 $e^{-}/Å^2$. For cGMP-unbound F403V-V407A mutant TAX-4/nanodisc sample, a total of 5,982 movies were collected at a nominal magnification of 130,000 ×, corresponding to a final pixel size of 1.06 Å. Each micrograph was dose-fractionated to 40 movie frames under a dose rate of 7.94 counts per pixel per second, with a total exposure time of 8 s and a frame exposure time of 0.2 s, resulting in a total dose of 56.45 $e^{-}/Å^2$. All micrographs were imaged from regions with an ice thickness range of 20-80 nm [64,65].

Image processing.

For all cryo-EM data collected, drift correction, beam-induced motion correction and dose -weighting were performed with MotionCor2 [66] using a 5 × 5 patch. The resulting integrated micrographs were used for further processing. Contrast-transfer function parameters of the micrographs were estimated using Gctf [67]. Particles were automatically picked by RELION 3.0 [68]. Initially, 617,269 and 801,931 particles were picked for cGMP-bound and -unbound WT TAX-4, respectively. The picked particles were 4 × binned (4.28 Å) and applied to two rounds of 2D classification and one round of 3D classification with *C1* symmetry. After the 2D and 3D classifications, a total of 128,685 particles for cGMP-bound WT TAX-4 and 163,525 particles for cGMP-unbound WT TAX-4 within classes exhibiting recognizable TAX-4 channel features were selected and re-extracted (1.07 Å) in RELION 3.0, and were then subjected to CryoSPARC [69] for 3D refinement with *C4* and *C1* symmetry individually. The final 3D cryo-EM density maps for cGMP-bound and -unbound WT TAX-4 in lipid nanodiscs were reconstructed and refined at 2.7 Å and 2.6 Å resolution with *C4* symmetry, and 2.9 Å and 2.8 Å resolution with *C1* symmetry. All resolutions were estimated by the gold-standard Fourier shell correlation (FSC) = 0.143 criterion. Local resolution was calculated using the built-in estimation in CryoSPARC. Image processing for F403V-V407A mutant TAX-4 was performed according to the same procedures described above. Initially 1,877,870 particles were picked; 445,131 particles were selected after 2D and 3D classifications. The final 3D cryo-EM density map was reconstructed and refined at 2.5 Å with *C4* symmetry and 2.7 Å with *C1* symmetry.

Model building, refinement, and validation.

For cGMP-bound WT TAX-4/nanodisc complex, the previously solved structure of TAX-4 in amphipol (PDB ID: 5H3O) was docked into the cryo-EM map constructed with *C4* symmetry using UCSF Chimera [70] to generate the initial model. For cGMP-unbound WT and F403V-V407A mutant TAX-4/nanodisc complexes, the structure of TAX-4 in amphipol (PDB ID: 5H3O) was modified by removing the cGMP molecules before docked into the corresponding cryo-EM maps (*C4* symmetry). All model building was conducted in Coot [71] using the real-space refinement tool by manual adjustment of main chain/side chain conformations that differed from the structure of TAX-4 in amphipol. 512 out of 733 residues were built for cGMP-bound WT TAX-4, and 513 out of 733 residues were built for cGMP-unbound WT and F403V-V407A mutant TAX-4. Residues 1-102, 161-166 and 621-733 in cGMP-bound WT TAX-4, and residues 1-103, 162-164 and 620-733 in cGMP-unbound WT and F403V-V407A mutant TAX-4 were not visible in the corresponding density maps. Coordinates and individual B-factors were refined against summed maps with secondary structure restraints and strict NCS constraints using phenix.real_space_refine [72] implemented in PHENIX [73]. Overfitting of the atomic models was validated via the previously described methods [74]. In brief, atoms in the final model were randomly shifted by up to 0.2 Å, and the new model was then refined against one of the two half maps generated during the final 3D reconstruction. FSC values were calculated between the map generated from the resulting model and the two half maps, as well as the averaged map of two half maps. The quality of the models were evaluated with MolProbity [75]. All the figures were prepared in PyMol [76] or UCSF Chimera [70].

Structural alignment and comparison.

Pair-wise structural superposition was performed with PyMol [76] by aligning all resolved atoms in the two tetramers. We opted to align all the atoms rather than a particular region and use four subunits rather than a single subunit for several reasons. (1) Our primary goal is to determine cGMP-induced conformational changes *in the full-length channel*. It is unknown *a priori* which regions of the channel do not undergo cGMP-induced conformational changes. Thus we believe that aligning all resolved atoms is more objective than selecting some atoms for alignment. (2) There is no experimental evidence to indicate that certain regions of the channel remain static upon cGMP binding/unbinding in the full-length channel. Thus, using a particular region for alignment seems arbitrary and lacks justification. (3) cGMP may produce tertiary conformational changes, which could be masked, undetected or under-measured in single subunit alignments. (4) The α-carbon r.m.s.d is 2.6 Å when the cGMP-unbound and -bound structures are superimposed based on an alignment of all resolved atoms. The r.m.s.d is 2.8 Å, 2.8 Å and 3.1 Å, respectively, if the alignment is based on S1-S3, S1-S6, or the β-roll of the CNBD. The all-atom alignment has the smallest r.m.s.d.

Molecular dynamics simulation and CHAP analysis.

To generate the input files for CHAP [30] analysis, all-atom molecular dynamics simulation (MDS) systems were built with the CHARMM-GUI [77] web server using CHARMM36 force field, based on the structures of cGMP-bound WT TAX-4, cGMP-unbound WT TAX-4, and

cGMP-unbound F403V-V407A mutant TAX-4. The structures were merged to a lipid bilayer composed of 512 1-Palmitoyl-2-oleoyl-sn-glycero-3-phosphocholine (POPC) molecules, and the systems were then solvated with 87337 TIP3P water molecules. 0.1 M NaCl was used to neutralize the systems, resulting in a total of ~365,000 atoms with initial dimensions of 147 Å × 147 Å × 167 Å.

CHAP analysis was performed according to online instructions (https://www.channotation.org) and personal communication with S. Tucker and G. Klesse. The PDB files generated by MDS were used as input for CHAP analysis. The output files of this analysis include the topology of the ion permeation pathway, pore radii, water densities and water free energies.

Electrophysiology.

For whole-cell recordings, human embryonic kidney (HEK) 293T cells (American Type Culture Collection (ATCC), not tested for mycoplasma) were grown in DMEM (Thermo Fisher Scientific) plus 10% Fetal bovine serum (Gibco) and penicillin (100 U/mL)/streptomycin (0.1 mg/mL) (Biological Industries). HEK 293T cells were transfected with WT or mutant TAX-4 using LipoD293 (SignaGen Laboratories) and used for recording in 48 h after transfection.

All experiments were performed at room temperature (~ 22 °C). Pipettes were fabricated from borosilicate glass (World Precision Instruments) using a micropipette puller (P-1000, Sutter Instrument), and were fire-polished to resistances of 3-4 MΩ for whole-cell recording. Whole-cell currents were elicited by 30-ms voltage steps from −100 mV to +150 mV with 10-mV increments, with a holding potential of 0 mV. Currents were amplified by Axopatch 200B and digitized by Digidata 1440A (Molecular Devices). Currents were low-pass filtered at 2 kHz and sampled at 10 kHz. pCLAMP 10 software (Molecular Devices) was used for data acquisition and analysis. Both intracellular and extracellular solutions contained (in mM) 140 NaCl, 5 KCl, 1 EGTA and 10 HEPES (pH 7.4 adjusted with NaOH). The EC_{50} of cGMP activation of TAX-4 is 0.16 μM in inside-out patch recordings from HEK 293T cells [10]. To ensure full activation of WT and mutant channels, a high concentration of 100 μM cGMP was added to the pipette solution.

For inside-out patch-clamp recordings on giant unilamellar vesicles (GUV), purified WT or F403V-V407A mutant TAX-4 proteins were reconstituted at a 1:100 (w/w) ratio into preformed Triton X-100 (0.11 % [w/v])-destabilized liposomes that were prepared from Brain Extract Polar (Avanti Polar Lipid) in 150 mM NaCl and 20 mM HEPES (pH 7.5) as described [78]. Triton X-100 was subsequently removed by Bio-Beads SM-2 (Bio-Rad). Three μl of reconstituted proteoliposomes was dehydrated on a clean cover slip overnight at 4°C. The dried proteoliposome layer was then rehydrated at room temperature with a standard bath solution containing (in mM) 270 NaCl, 30 KCl and 10 HEPES 10 (pH 7.5 adjusted with NaOH) to form GUV. For single-channel recording, patch pipettes were pulled from Borosilicate glass (Harvard Apparatus) and had a resistance of 5-7 MΩ when filled with a solution containing (in mM) 270 NaCl, 30 KCl and 10 HEPES 10 (pH 7.5 adjusted with NaOH). Giga-Ω seal was formed by gentle suction when the patch pipette made contact with the GUV. To obtain an inside-out single layer of membrane patch, the pipette was pulled

away from the GUV and the tip was exposed to air for 1-2 seconds and put back into the standard bath solution. Data were acquired by AxoPatch 200B and digitized by Digidata 1322A. Currents were low-pass filtered at 1 kHz and sampled at 50 kHz. pCLAMP 9 software was used for data acquisition and analysis. To elicit single-channel currents, 0.5-5 uM cGMP was added to the bath solution.

Immunofluorescence and imaging.

HEK 293T cells were plated on poly-D-lysine-coated (Sigma) glass coverslips in DMEM (Invitrogen) supplemented with 10% fetal bovine serum (Hyclone), and kept in an incubator at 37 °C in a 5% CO_2 humid atmosphere. Transfection was performed using Lipofectamine 2000 (Invitrogen) according to the manufacturer's instructions. 2.5 μg of GFP-TAX-4_WT-HA or corresponding mutants cDNAs in 200 μl Opti-MEM (Invitrogen) were used to transfect each 12 mm (diameter) coverslip.

Immunofluorescence staining was performed 36 h post-transfection, at which time GFP's expression was seen to peak. The culture medium was removed, and the transfected cells were briefly rinsed with PBS, and immediately fixed with PBS supplemented with 2% paraformaldehyde-4% sucrose, for 15 min at room temperature. Cells were then washed in PBS, and subsequently blocked in a non-permeabilizing (detergent-free) blocking buffer, which consisted of 1% fish gelatin (Sigma) and 2% goat serum (Sigma) in PBS, for 4 h at room temperature. To visualize surface HA tags, the fixed cells were incubated with a primary antibody against HA (mouse monoclonal anti-HA, BioLegend) at 4ºC overnight (diluted in blocking buffer, 1:160), then washed with PBS four times. A goat anti-mouse secondary antibody conjugated with the Alexa594 fluorophore (Life Technologies) was added to the coverslips for 1.5 h at room temperature (in blocking buffer, 1:700). The stained coverslips were finally washed 5 times with PBS before imaging.

Imaging was performed using a spinning disc confocal microscope, built on an inverted Nikon Eclipse TE2000-S microscope. Optics consisted of a spinning disc scanner unit (CSU10, Yokogawa) and a CCD high resolution digital ImageM camera (Hamamatsu). Images were acquired using a 60x color-corrected objective lens (Nikon). The GFP (green) laser line used 491 nm and 520 nm as excitation and emission wavelengths, respectively. The Alexa594 (red) laser optical path consisted of a 561 nm excitation source and a 591 nm emission filter. Laser sources and equipment were from Spectral. Optical filters (Chroma) were sputter-coated, to minimize chromatic aberration.

Focal plane thickness (z-axis) was 200 nm in all conditions. Confocal images for each fluorophore (GFP and HA) were always acquired as sequential scans (every 200 nm), which eliminated any optical bleed-through for the fluorophores used. Images were acquired and analyzed with Volocity 6.3 (PerkinElmer).

Statistics and reproducibility.

Blind experiments were conducted in HEK 293T whole-cell recordings with independent biological replicates. The homogeneity of variance was first tested using Levene's Test. Based on the result of Levene's Test, statistical significance was evaluated using two-tailed t-test (for all two-group comparisons). Data are presented as the mean ± standard error of the

mean (s.e.m.). A p-value of < 0.05 is considered statistically significant and is denoted by *, and “ns” indicates no significant difference.

CHAP analysis in Figs. 2c,d and 4f,g was repeated twice independently and the results were identical. Gel-filtration, SDS-PAGE and 2D classification in Extended Data Figs. 1, 3 and 4 were performed independently at least three times and the results were consistent.

Cell lines.

Sf9 (Invitrogen) and HEK 293T (ATCC) cells were used. Cell lines were not authenticated or tested for mycoplasma contamination.

Reporting summary.

Further information on experimental design is available in the Nature Research Reporting Summary linked to this article.

Data availability

The cryo-EM density maps have been deposited in the Electron Microscopy Data Bank under the accession number EMD-21649 for cGMP-unbound WT TAX-4, EMD-21650 for cGMP-bound WT TAX-4, and EMD-21651 for cGMP-unbound F403V-V407A mutant TAX-4. The coordinates of the atomic models have been deposited in the Protein Data Bank under the accession number 6WEJ for cGMP-unbound WT TAX-4, 6WEK for cGMP-bound WT TAX-4, and 6WEL for cGMP-unbound F403V-V407A mutant TAX-4. Source data for Fig. 4a,b and Extended Data Figs, 1b, 3b and 4b are available with the paper online.

Extended Data

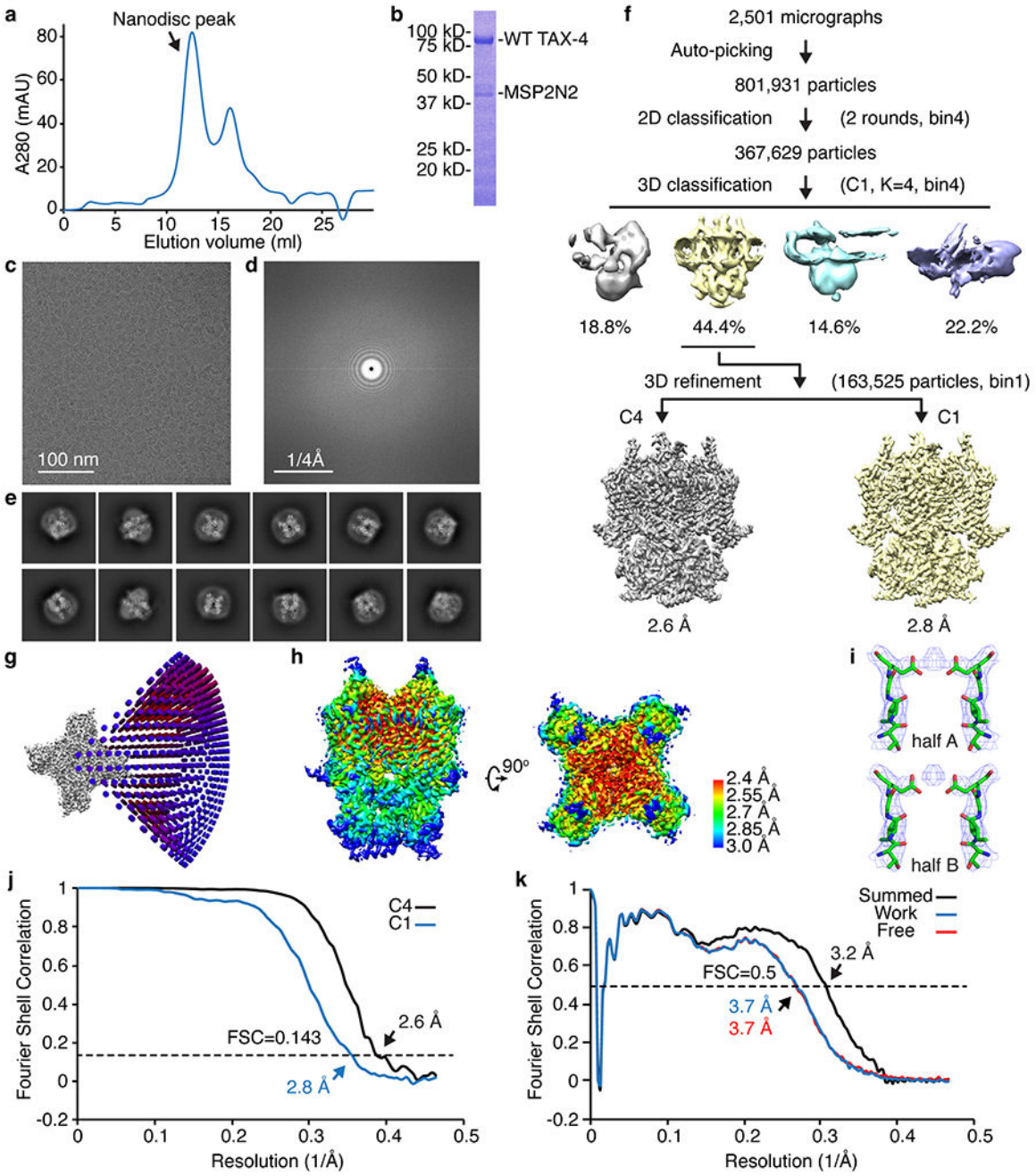

Extended Data Fig 1. Cryo-EM single-particle analysis of cGMP-unbound TAX-4 reconstituted in lipid nanodiscs.

a, Gel filtration profile of cGMP-unbound TAX-4 nanodisc sample. **b**, SDS-PAGE of cGMP-unbound TAX-4 nanodisc sample used for cryo-EM. Unprocessed gel is available as source data. **c**, A representative motion-corrected micrograph. **d**, Fourier power spectrum of the micrograph shown in (**c**). **e**, Gallery of typical averages from 2D classification. **f**, Flow chart of cryo-EM image processing. **g**, Euler angle distribution of particles used in the final 3D reconstruction with C4 symmetry. **h**, Local resolution of the final density map

reconstructed with C4 symmetry. **i**, Densities of the SF generated from the two half maps, contoured at 5σ and overlaid with the model. **j**, Gold-standard FSC curves of the final 3D reconstructions with C4 and C1 symmetry, respectively. **k**, FSC curves for cross-validation between maps and model. Black, model versus the summed map. Blue, model versus the half map that was used for model refinement (called ‘work’). Red, model versus another half map that was not used for model refinement (called ‘free’). Uncropped image for panel **b** is available as source data

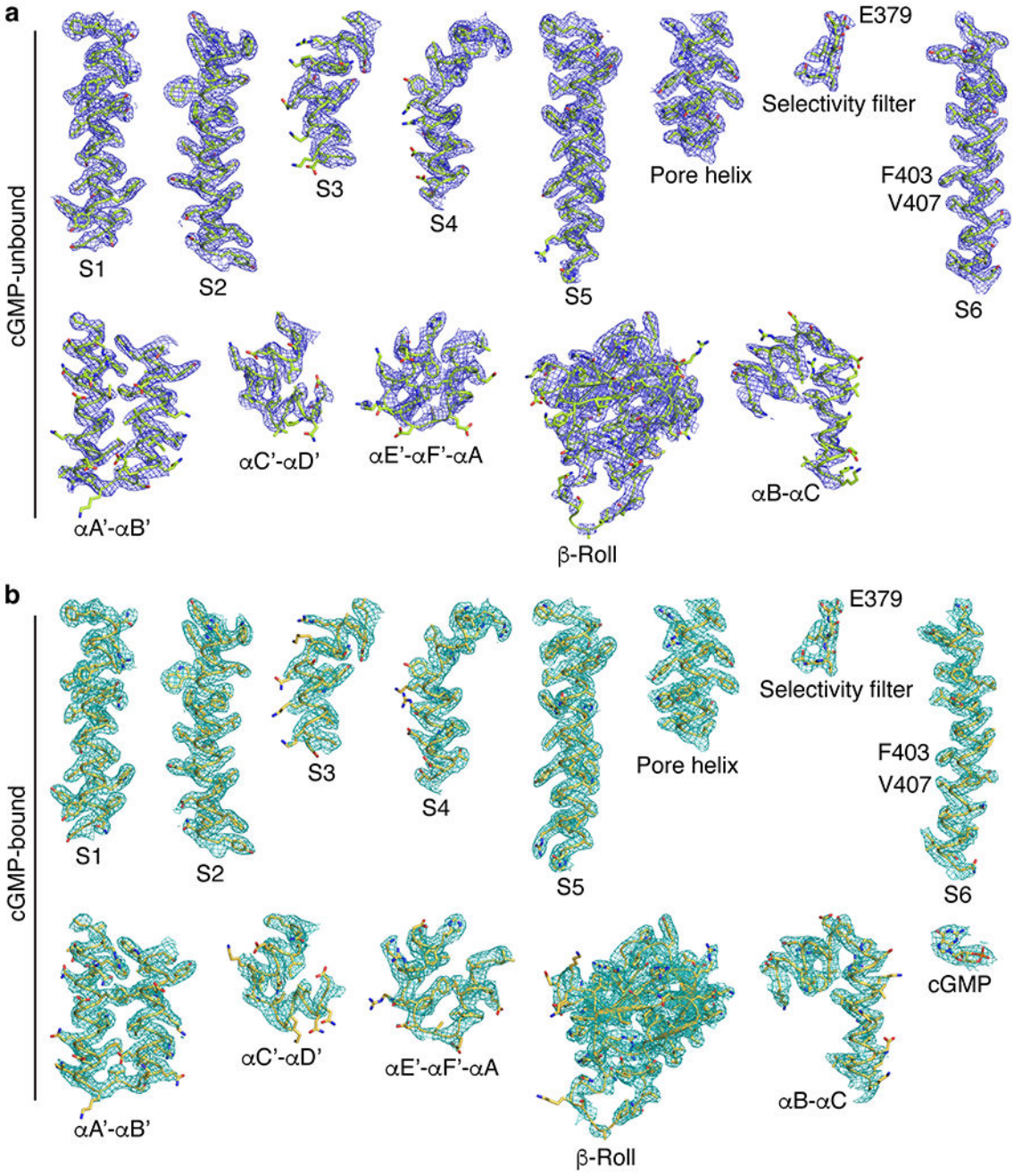

Extended Data Fig 2. Cryo-EM density maps and atomic models of selected key regions in cGMP-unbound and -bound structures.

a, cGMP-unbound. The map was low-pass filtered to 2.6 Å, sharpened with a temperature factor of −117 Å^2 and contoured at 5σ. **b**, cGMP-bound. The map was low-pass filtered to 2.7 Å, sharpened with a temperature factor of −113 Å^2 and contoured at 5σ

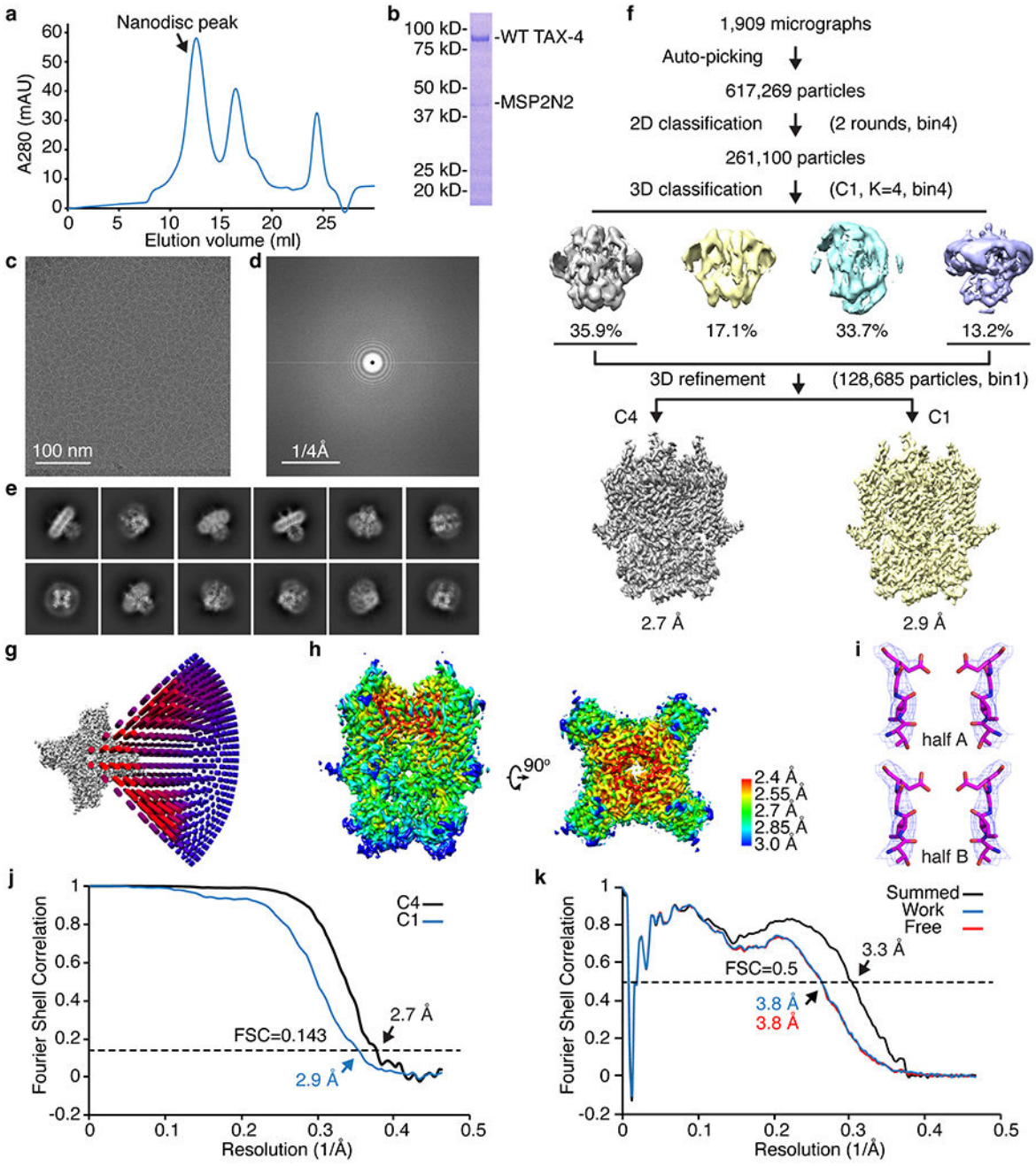

Extended Data Fig 3. Cryo-EM single-particle analysis of cGMP-bound TAX-4 reconstituted in lipid nanodiscs.

a, Gel filtration profile of cGMP-bound TAX-4 nanodisc sample. **b**, SDS-PAGE of cGMP-bound TAX-4 nanodisc sample used for cryo-EM. Unprocessed gel is available as source data. **c**, A representative motion-corrected micrograph. **d**, Fourier power spectrum of the micrograph shown in (**c**). **e**, Gallery of typical averages from 2D classification. **f**, Flow chart of cryo-EM image processing. **g**, Euler angle distribution of particles used in the final 3D reconstruction with C4 symmetry. **h**, Local resolution of the final density map reconstructed

with C4 symmetry. **i**, Densities of the SF generated from the two half maps, contoured at 5σ and overlaid with the model. **j**, Gold-standard FSC curves of the final 3D reconstructions with C4 and C1 symmetry, respectively. **k**, FSC curves for cross-validation between maps and model. Black, model versus the summed map. Blue, model versus the half map that was used for model refinement (called ‘work’). Red, model versus another half map that was not used for model refinement (called ‘free’). Uncropped image for panel **b** is available as source data

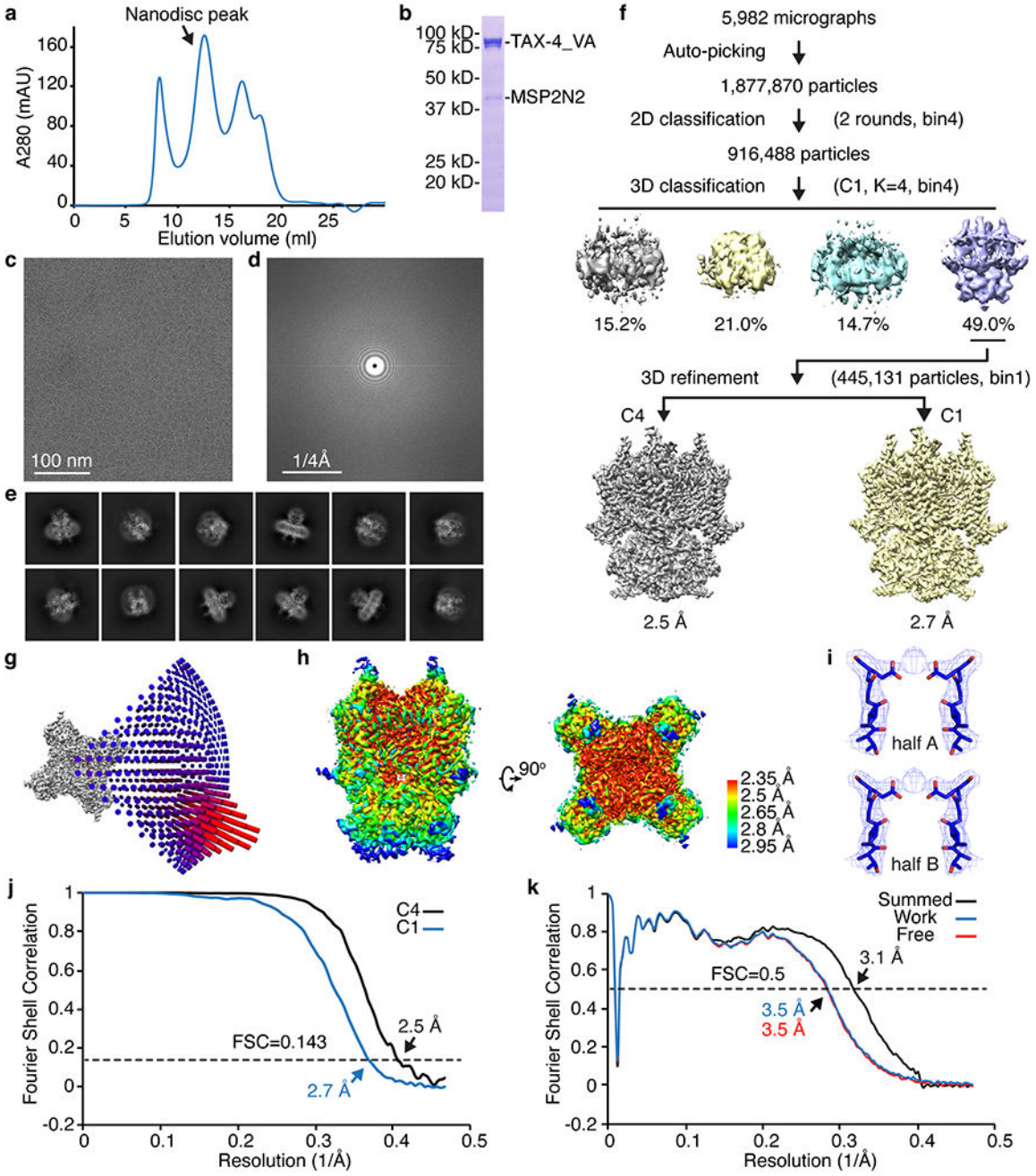

Extended Data Fig 4. Cryo-EM single-particle analysis of cGMP-unbound F403V-V407A (VA) mutant TAX-4 reconstituted in lipid nanodiscs.

a, Gel filtration profile of cGMP-bound VA TAX-4 nanodisc sample. **b**, SDS-PAGE of cGMP-bound VA TAX-4 nanodisc sample used for cryo-EM. Unprocessed gel is available as source data. **c**, A representative motion-corrected micrograph. **d**, Fourier power spectrum of the micrograph shown in (**c**). **e**, Gallery of typical averages from 2D classification. **f**, Flow chart of cryo-EM image processing. **g**, Euler angle distribution of particles used in the final 3D reconstruction with C4 symmetry. **h**, Local resolution of the final density map

reconstructed with C4 symmetry. **i**, Densities of the SF generated from the two half maps, contoured at 5σ and overlaid with the model. **j**, Gold-standard FSC curves of the final 3D reconstructions with C4 and C1 symmetry, respectively. **k**, FSC curves for cross-validation between maps and model. Black, model versus the summed map. Blue, model versus the half map that was used for model refinement (called ‘work’). Red, model versus another half map that was not used for model refinement (called ‘free’). Uncropped image for panel **b** is available as source data

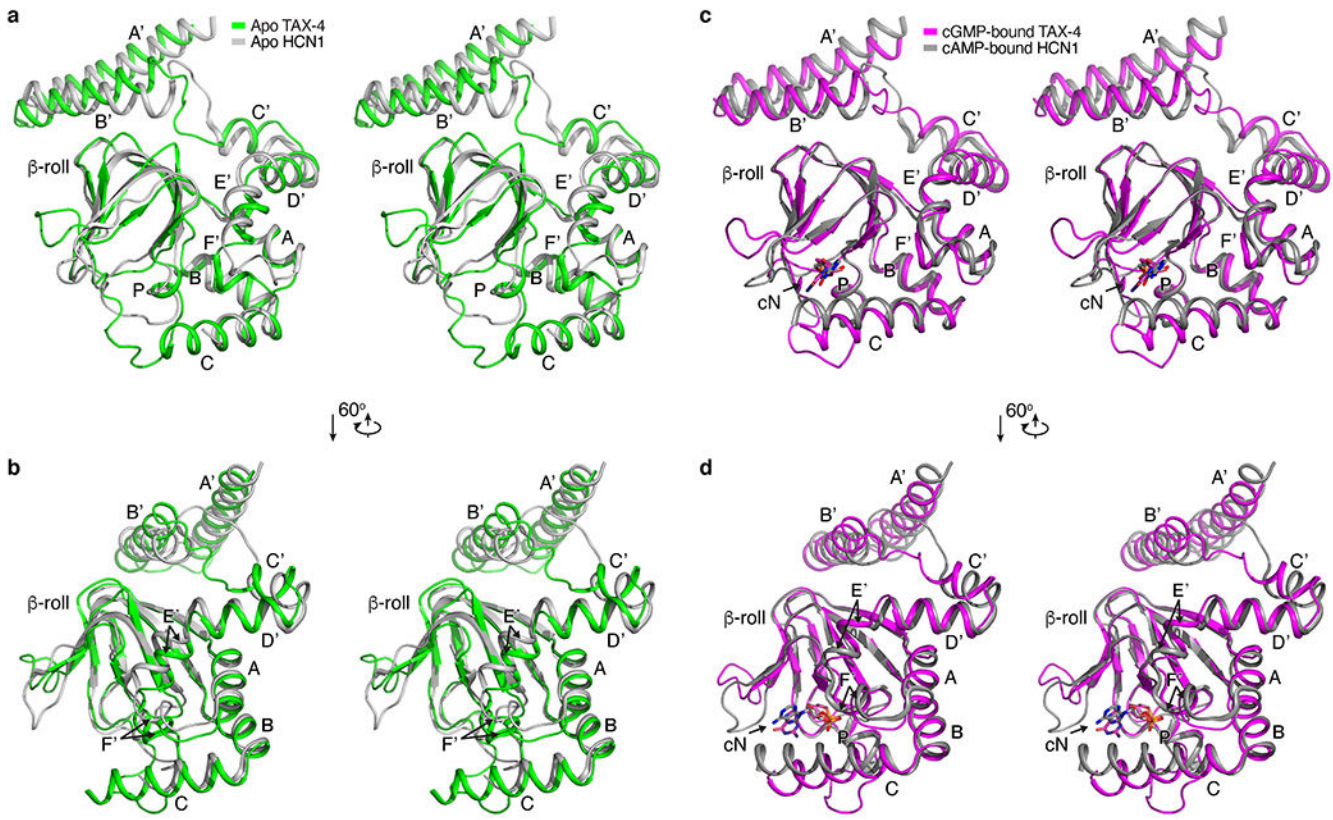

Extended Data Fig 5. Comparison of the CNBD and C-linker structures of TAX-4 and HCN1.

a,b, Superposition of the CNBD and C-linker structures in unliganded states in stereo view. The α-carbon r.m.s.d is 9.2 Å. **c**,**d**, Superposition of the CNBD and C-linker structures in liganded states in stereo view. The α-carbon r.m.s.d is 9.4 Å

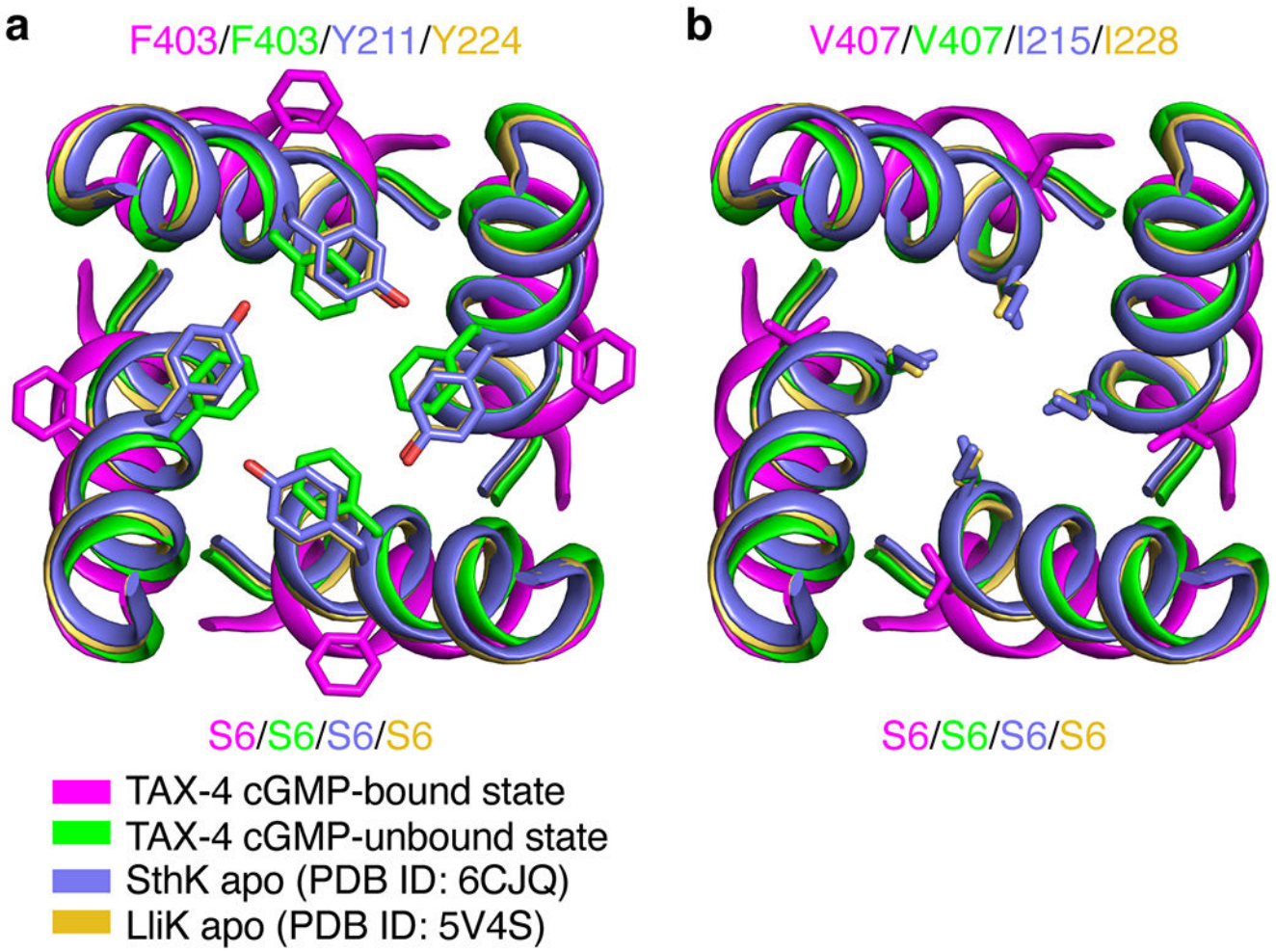

Extended Data Fig 6. Superposition of S6 of TAX-4 orthologs.

a,b, Superposition of S6 (viewed from the extracellular side) of cGMP-bound (open state) TAX-4, apo (closed state) TAX-4, apo SthK (PDB ID: 6CJQ) and apo LliK (PDB ID: 5V4S), showing the presence of a hydrophobic cavity gate in all the apo structures

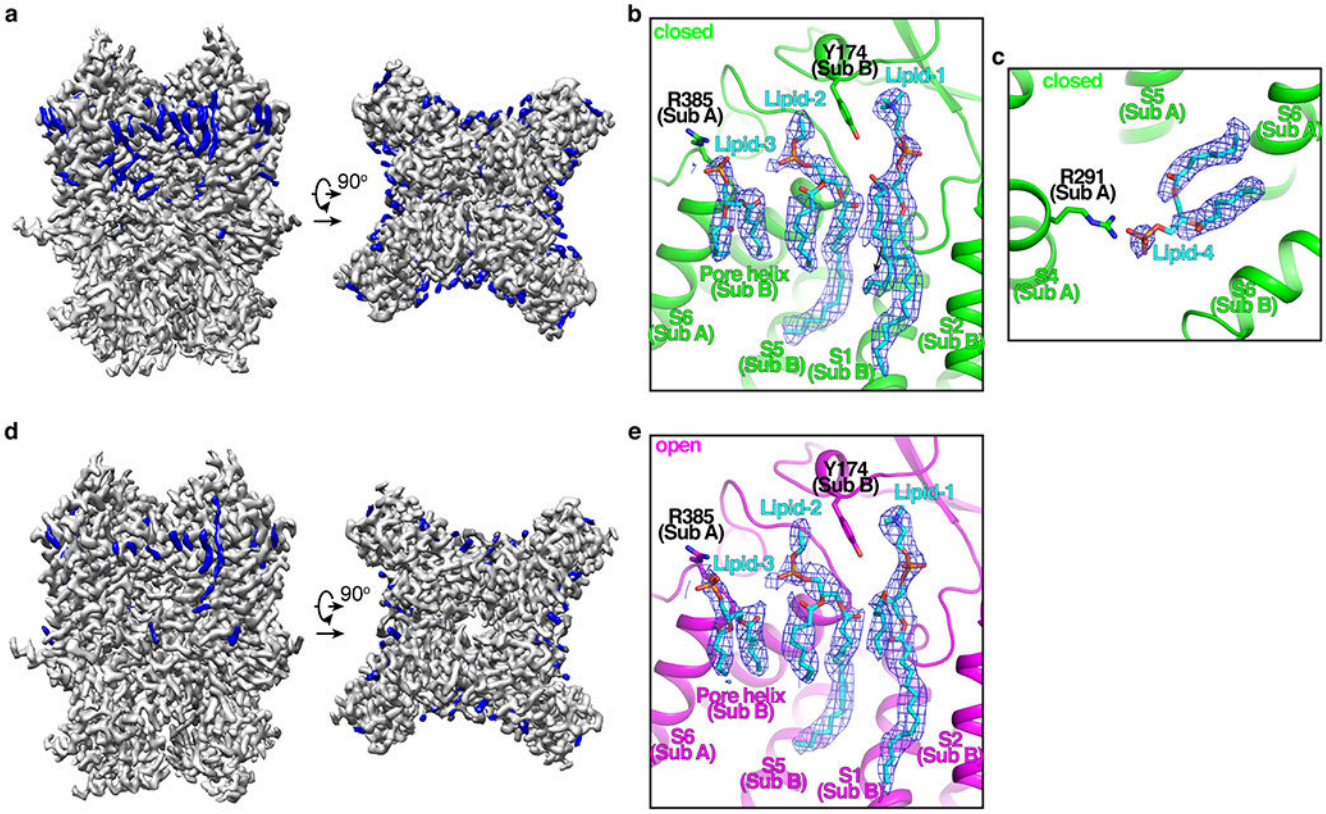

Extended Data Fig 7. TAX-4 and lipid interactions.

a, Cryo-EM density map of cGMP-unbound TAX-4 reconstituted in lipid nanodiscs. Densities colored in blue are not modeled into TAX-4 and likely represent lipids. **b,c**, Possible lipid binding in several different regions in the closed state. The extra densities were fit with phosphatidylcholine (lipid 1 and 2) or phosphatidic acid (lipid 3 and 4). **d**, Cryo-EM density map of cGMP-bound TAX-4 reconstituted in lipid nanodiscs. Densities colored in blue are not modeled into TAX-4 and likely represent lipids. **e**, Possible lipid binding in the open state. The extra densities were fit with phosphatidylcholine (lipid 1 and 2) or phosphatidic acid (lipid 3). Density maps were contoured at 5σ (**b,e**) or 3σ (**c**).

Supplementary Material

Refer to Web version on PubMed Central for supplementary material.

ACKNOWLEDGMENTS

We thank S. Tucker and G. Klesse (University of Oxford) for assisting the installation and use of CHAP and developing a new CHAP module for this work, K. Zhang (Yale University) and Z. Li (Purdue University) for discussion on structure validation, B. Carragher and C. Potter for access to and L. Yen and E. Eng for help with the use of the electron microscopy facility at the New York Structural Biology Center (NYSBC). This work was supported by grants to J.Y. from the National Institutes of Health (NIH) (RO1EY027800 and R01GM085234), to J.F. from the NIH (R01GM055440), to G.L. from the National Natural Science Foundation of China (NSFC) (21625302 and 21933010), and to Y.Z. from the NSFC (31700647) and the Strategic Priority Research Program of the Chinese Academy of Sciences (XDB17000000). Some of the cryo-EM work was performed at the Simons Electron Microscopy Center and National Resource for Automated Molecular Microscopy located at NYSBC, supported by grants from the Simons Foundation (SF349247), NYSTAR, and the NIH National Institute of General

Medical Sciences (GM103310) with additional support from Agouron Institute (F00316) and NIH (OD019994). Some cryo-EM work was performed at the National Center for CryoEM Access and Training (NCCAT) and the Simons Electron Microscopy Center located at NYSBC, supported by the NIH Common Fund Transformative High Resolution Cryo-Electron Microscopy program (U24 GM129539,) and by grants from the Simons Foundation (SF349247) and NY State Assembly Majority.

References

1. Kaupp UB & Seifert R Cyclic nucleotide-gated ion channels. Physiol Rev 82, 769–824, doi:10.1152/physrev.00008.2002 (2002). [PubMed: 12087135]
2. Zagotta WN & Siegelbaum SA Structure and function of cyclic nucleotide-gated channels. Annu Rev Neurosci 19, 235–263, doi:10.1146/annurev.ne.19.030196.001315 (1996). [PubMed: 8833443]
3. Varnum MD & Dai G in The Hankbook of Ion Channels (eds Zheng J & Trudeau MC) 361–382 (CRC Press, 2015).
4. Michalakis S, Becirovic E & Biel M Retinal Cyclic Nucleotide-Gated Channels: From Pathophysiology to Therapy. Int J Mol Sci 19, doi:10.3390/ijms19030749 (2018).
5. Fesenko EE, Kolesnikov SS & Lyubarsky AL Induction by cyclic GMP of cationic conductance in plasma membrane of retinal rod outer segment. Nature 313, 310–313 (1985). [PubMed: 2578616]
6. Nakamura T & Gold GH A cyclic nucleotide-gated conductance in olfactory receptor cilia. Nature 325, 442–444, doi:10.1038/325442a0 (1987). [PubMed: 3027574]
7. Kaupp UB et al. Primary structure and functional expression from complementary DNA of the rod photoreceptor cyclic GMP-gated channel. Nature 342, 762–766, doi:10.1038/342762a0 (1989). [PubMed: 2481236]
8. Dhallan RS, Yau KW, Schrader KA & Reed RR Primary structure and functional expression of a cyclic nucleotide-activated channel from olfactory neurons. Nature 347, 184–187, doi:10.1038/347184a0 (1990). [PubMed: 1697649]
9. Goulding EH, Tibbs GR, Liu D & Siegelbaum SA Role of H5 domain in determining pore diameter and ion permeation through cyclic nucleotide-gated channels. Nature 364, 61–64, doi:10.1038/364061a0 (1993). [PubMed: 7686276]
10. Li M et al. Structure of a eukaryotic cyclic-nucleotide-gated channel. Nature 542, 60–65, doi:10.1038/nature20819 (2017). [PubMed: 28099415]
11. Gordon SE & Zagotta WN A histidine residue associated with the gate of the cyclic nucleotide-activated channels in rod photoreceptors. Neuron 14, 177–183 (1995). [PubMed: 7530019]
12. Gordon SE & Zagotta WN Localization of regions affecting an allosteric transition in cyclic nucleotide-activated channels. Neuron 14, 857–864 (1995). [PubMed: 7536427]
13. Brown RL, Snow SD & Haley TL Movement of gating machinery during the activation of rod cyclic nucleotide-gated channels. Biophys J 75, 825–833 (1998). [PubMed: 9675183]
14. Zong X, Zucker H, Hofmann F & Biel M Three amino acids in the C-linker are major determinants of gating in cyclic nucleotide-gated channels. EMBO J 17, 353–362, doi:10.1093/emboj/17.2.353 (1998). [PubMed: 9430627]
15. Zhou L, Olivier NB, Yao H, Young EC & Siegelbaum SA A conserved tripeptide in CNG and HCN channels regulates ligand gating by controlling C-terminal oligomerization. Neuron 44, 823–834, doi:10.1016/j.neuron.2004.11.012 (2004). [PubMed: 15572113]
16. Paoletti P, Young EC & Siegelbaum SA C-Linker of cyclic nucleotide-gated channels controls coupling of ligand binding to channel gating. J Gen Physiol 113, 17–34 (1999). [PubMed: 9874685]
17. Flynn GE & Zagotta WN Conformational changes in S6 coupled to the opening of cyclic nucleotide-gated channels. Neuron 30, 689–698 (2001). [PubMed: 11430803]
18. Contreras JE & Holmgren M Access of quaternary ammonium blockers to the internal pore of cyclic nucleotide-gated channels: implications for the location of the gate. J Gen Physiol 127, 481–494, doi:10.1085/jgp.200509440 (2006). [PubMed: 16606688]
19. Contreras JE, Srikumar D & Holmgren M Gating at the selectivity filter in cyclic nucleotide-gated channels. Proc Natl Acad Sci U S A 105, 3310–3314, doi:10.1073/pnas.0709809105 (2008). [PubMed: 18287006]

20. Sun ZP, Akabas MH, Goulding EH, Karlin A & Siegelbaum SA Exposure of residues in the cyclic nucleotide-gated channel pore: P region structure and function in gating. Neuron 16, 141–149 (1996). [PubMed: 8562078]
21. Becchetti A & Roncaglia P Cyclic nucleotide-gated channels: intra- and extracellular accessibility to Cd2+ of substituted cysteine residues within the P-loop. Pflugers Arch 440, 556–565 (2000). [PubMed: 10958339]
22. James ZM & Zagotta WN Structural insights into the mechanisms of CNBD channel function. J Gen Physiol 150, 225–244, doi:10.1085/jgp.201711898 (2018). [PubMed: 29233886]
23. Flynn GE, Johnson JP Jr. & Zagotta WN Cyclic nucleotide-gated channels: shedding light on the opening of a channel pore. Nat Rev Neurosci 2, 643–651, doi:10.1038/35090015 (2001). [PubMed: 11533732]
24. Cukkemane A, Seifert R & Kaupp UB Cooperative and uncooperative cyclic-nucleotide-gated ion channels. Trends Biochem Sci 36, 55–64, doi:10.1016/j.tibs.2010.07.004 (2011). [PubMed: 20729090]
25. Clayton GM, Altieri S, Heginbotham L, Unger VM & Morais-Cabral JH Structure of the transmembrane regions of a bacterial cyclic nucleotide-regulated channel. Proc Natl Acad Sci U S A 105, 1511–1515, doi:10.1073/pnas.0711533105 (2008). [PubMed: 18216238]
26. James ZM et al. CryoEM structure of a prokaryotic cyclic nucleotide-gated ion channel. Proc Natl Acad Sci U S A 114, 4430–4435, doi:10.1073/pnas.1700248114 (2017). [PubMed: 28396445]
27. Rheinberger J, Gao X, Schmidpeter PA & Nimigean CM Ligand discrimination and gating in cyclic nucleotide-gated ion channels from apo and partial agonist-bound cryo-EM structures. Elife 7, doi:10.7554/eLife.39775 (2018).
28. Komatsu H, Mori I, Rhee JS, Akaike N & Ohshima Y Mutations in a cyclic nucleotide-gated channel lead to abnormal thermosensation and chemosensation in C. elegans. Neuron 17, 707–718, doi:S0896-6273(00)80202-0 [pii] (1996). [PubMed: 8893027]
29. Komatsu H et al. Functional reconstitution of a heteromeric cyclic nucleotide-gated channel of Caenorhabditis elegans in cultured cells. Brain Res 821, 160–168, doi:S0006-8993(99)01111-7 [pii] (1999). [PubMed: 10064800]
30. Klesse G, Rao S, Sansom MSP & Tucker SJ CHAP: A Versatile Tool for the Structural and Functional Annotation of Ion Channel Pores. J Mol Biol 431, 3353–3365, doi:10.1016/j.jmb.2019.06.003 (2019). [PubMed: 31220459]
31. Rao S, Klesse G, Stansfeld PJ, Tucker SJ & Sansom MSP A heuristic derived from analysis of the ion channel structural proteome permits the rapid identification of hydrophobic gates. Proc Natl Acad Sci U S A 116, 13989–13995, doi:10.1073/pnas.1902702116 (2019). [PubMed: 31235590]
32. Trick JL et al. Functional Annotation of Ion Channel Structures by Molecular Simulation. Structure 24, 2207–2216, doi:10.1016/j.str.2016.10.005 (2016). [PubMed: 27866853]
33. Doyle DA et al. The structure of the potassium channel: molecular basis of K+ conduction and selectivity. Science 280, 69–77 (1998). [PubMed: 9525859]
34. Cao E, Liao M, Cheng Y & Julius D TRPV1 structures in distinct conformations reveal activation mechanisms. Nature 504, 113–118, doi:nature12823 [pii] 10.1038/nature12823 (2013). [PubMed: 24305161]
35. Lee CH & MacKinnon R Structures of the Human HCN1 Hyperpolarization-Activated Channel. Cell 168, 111–120 e111, doi:10.1016/j.cell.2016.12.023 (2017). [PubMed: 28086084]
36. Flynn GE & Zagotta WN A cysteine scan of the inner vestibule of cyclic nucleotide-gated channels reveals architecture and rearrangement of the pore. J Gen Physiol 121, 563–582, doi:10.1085/jgp.200308819 (2003). [PubMed: 12771192]
37. Zagotta WN et al. Structural basis for modulation and agonist specificity of HCN pacemaker channels. Nature 425, 200–205, doi:10.1038/nature01922 (2003). [PubMed: 12968185]
38. Saponaro A et al. Structural basis for the mutual antagonism of cAMP and TRIP8b in regulating HCN channel function. Proc Natl Acad Sci U S A 111, 14577–14582, doi:1410389111 [pii] 10.1073/pnas.1410389111 (2014). [PubMed: 25197093]
39. Xu X, Vysotskaya ZV, Liu Q & Zhou L Structural basis for the cAMP-dependent gating in the human HCN4 channel. J Biol Chem 285, 37082–37091, doi:10.1074/jbc.M110.152033 (2010). [PubMed: 20829353]

40. Lolicato M et al. Tetramerization dynamics of C-terminal domain underlies isoform-specific cAMP gating in hyperpolarization-activated cyclic nucleotide-gated channels. J Biol Chem 286, 44811–44820, doi:10.1074/jbc.M111.297606 (2011). [PubMed: 22006928]
41. Taraska JW, Puljung MC, Olivier NB, Flynn GE & Zagotta WN Mapping the structure and conformational movements of proteins with transition metal ion FRET. Nat Methods 6, 532–537, doi:10.1038/nmeth.1341 (2009). [PubMed: 19525958]
42. Altieri SL et al. Structural and energetic analysis of activation by a cyclic nucleotide binding domain. J Mol Biol 381, 655–669, doi:10.1016/j.jmb.2008.06.011 (2008). [PubMed: 18619611]
43. Goldschen-Ohm MP et al. Structure and dynamics underlying elementary ligand binding events in human pacemaking channels. Elife 5, doi:10.7554/eLife.20797 (2016).
44. Kowal J et al. Ligand-induced structural changes in the cyclic nucleotide-modulated potassium channel MloK1. Nat Commun 5, 3106, doi:10.1038/ncomms4106 (2014). [PubMed: 24469021]
45. Marchesi A et al. An iris diaphragm mechanism to gate a cyclic nucleotide-gated ion channel. Nat Commun 9, 3978, doi:10.1038/s41467-018-06414-8 (2018). [PubMed: 30266906]
46. Kim DM & Nimigean CM Voltage-Gated Potassium Channels: A Structural Examination of Selectivity and Gating. Cold Spring Harb Perspect Biol 8, doi:10.1101/cshperspect.a029231 (2016).
47. Zhou X et al. Cryo-EM structures of the human endolysosomal TRPML3 channel in three distinct states. Nat Struct Mol Biol 24, 1146–1154, doi:10.1038/nsmb.3502 (2017). [PubMed: 29106414]
48. Fodor AA, Black KD & Zagotta WN Tetracaine reports a conformational change in the pore of cyclic nucleotide-gated channels. J Gen Physiol 110, 591–600 (1997). [PubMed: 9348330]
49. Fodor AA, Gordon SE & Zagotta WN Mechanism of tetracaine block of cyclic nucleotide-gated channels. J Gen Physiol 109, 3–14 (1997). [PubMed: 8997661]
50. Craven KB, Olivier NB & Zagotta WN C-terminal movement during gating in cyclic nucleotide-modulated channels. J Biol Chem 283, 14728–14738, doi:10.1074/jbc.M710463200 (2008). [PubMed: 18367452]
51. Craven KB & Zagotta WN Salt bridges and gating in the COOH-terminal region of HCN2 and CNGA1 channels. J Gen Physiol 124, 663–677, doi:10.1085/jgp.200409178 (2004). [PubMed: 15572346]
52. Mazzolini M et al. The gating mechanism in cyclic nucleotide-gated ion channels. Sci Rep 8, 45, doi:10.1038/s41598-017-18499-0 (2018). [PubMed: 29311674]
53. Martinez-Francois JR, Xu Y & Lu Z Mutations reveal voltage gating of CNGA1 channels in saturating cGMP. J Gen Physiol 134, 151–164, doi:10.1085/jgp.200910240 (2009). [PubMed: 19635856]
54. Mazzolini M, Anselmi C & Torre V The analysis of desensitizing CNGA1 channels reveals molecular interactions essential for normal gating. J Gen Physiol 133, 375–386, doi:10.1085/jgp.200810157 (2009). [PubMed: 19289572]
55. Crary JI, Dean DM, Nguitragool W, Kurshan PT & Zimmerman AL Mechanism of inhibition of cyclic nucleotide-gated ion channels by diacylglycerol. J Gen Physiol 116, 755–768 (2000). [PubMed: 11099345]
56. Womack KB et al. Do phosphatidylinositides modulate vertebrate phototransduction? J Neurosci 20, 2792–2799 (2000). [PubMed: 10751430]
57. Bright SR, Rich ED & Varnum MD Regulation of human cone cyclic nucleotide-gated channels by endogenous phospholipids and exogenously applied phosphatidylinositol 3,4,5-trisphosphate. Mol Pharmacol 71, 176–183, doi:10.1124/mol.106.026401 (2007). [PubMed: 17018579]
58. Spehr M, Wetzel CH, Hatt H & Ache BW 3-phosphoinositides modulate cyclic nucleotide signaling in olfactory receptor neurons. Neuron 33, 731–739 (2002). [PubMed: 11879650]
59. Zhainazarov AB, Spehr M, Wetzel CH, Hatt H & Ache BW Modulation of the olfactory CNG channel by Ptdlns(3,4,5)P3. J Membr Biol 201, 51–57 (2004). [PubMed: 15635812]
60. Gordon SE, Downing-Park J, Tam B & Zimmerman AL Diacylglycerol analogs inhibit the rod cGMP-gated channel by a phosphorylation-independent mechanism. Biophys J 69, 409–417, doi:10.1016/S0006-3495(95)79913-1 (1995). [PubMed: 8527654]

61. Dai G, Peng C, Liu C & Varnum MD Two structural components in CNGA3 support regulation of cone CNG channels by phosphoinositides. J Gen Physiol 141, 413–430, doi:10.1085/jgp.201210944 (2013). [PubMed: 23530136]
62. Ritchie TK et al. Chapter 11 - Reconstitution of membrane proteins in phospholipid bilayer nanodiscs. Methods Enzymol 464, 211–231, doi:10.1016/S0076-6879(09)64011-8 (2009). [PubMed: 19903557]
63. Suloway C et al. Automated molecular microscopy: the new Leginon system. J Struct Biol 151, 41–60, doi:10.1016/j.jsb.2005.03.010 (2005). [PubMed: 15890530]
64. Feng X et al. A Fast and Effective Microfluidic Spraying-Plunging Method for High-Resolution Single-Particle Cryo-EM. Structure 25, 663–670 e663, doi:10.1016/j.str.2017.02.005 (2017). [PubMed: 28286002]
65. Rice WJ et al. Routine determination of ice thickness for cryo-EM grids. J Struct Biol 204, 38–44, doi:10.1016/j.jsb.2018.06.007 (2018). [PubMed: 29981485]
66. Zheng SQ et al. MotionCor2: anisotropic correction of beam-induced motion for improved cryo-electron microscopy. Nat Methods 14, 331–332, doi:10.1038/nmeth.4193 (2017). [PubMed: 28250466]
67. Zhang K Gctf: Real-time CTF determination and correction. J Struct Biol 193, 1–12, doi:10.1016/j.jsb.2015.11.003 (2016). [PubMed: 26592709]
68. Zivanov J et al. New tools for automated high-resolution cryo-EM structure determination in RELION-3. Elife 7, doi:10.7554/eLife.42166 (2018).
69. Punjani A, Rubinstein JL, Fleet DJ & Brubaker MA cryoSPARC: algorithms for rapid unsupervised cryo-EM structure determination. Nat Methods 14, 290–296, doi:10.1038/nmeth.4169 (2017). [PubMed: 28165473]
70. Pettersen EF et al. UCSF Chimera--a visualization system for exploratory research and analysis. J Comput Chem 25, 1605–1612, doi:10.1002/jcc.20084 (2004). [PubMed: 15264254]
71. Emsley P & Cowtan K Coot: model-building tools for molecular graphics. Acta Crystallogr D Biol Crystallogr 60, 2126–2132, doi:10.1107/S0907444904019158 (2004). [PubMed: 15572765]
72. Afonine PV et al. Real-space refinement in PHENIX for cryo-EM and crystallography. Acta Crystallogr D Struct Biol 74, 531–544, doi:10.1107/S2059798318006551 (2018). [PubMed: 29872004]
73. Adams PD et al. PHENIX: a comprehensive Python-based system for macromolecular structure solution. Acta Crystallogr D Biol Crystallogr 66, 213–221, doi:S0907444909052925 [pii] 10.1107/S0907444909052925 (2010). [PubMed: 20124702]
74. Amunts A et al. Structure of the yeast mitochondrial large ribosomal subunit. Science 343, 1485–1489, doi:343/6178/1485 [pii] 10.1126/science.1249410 (2014). [PubMed: 24675956]
75. Chen VB et al. MolProbity: all-atom structure validation for macromolecular crystallography. Acta Crystallogr D Biol Crystallogr 66, 12–21, doi:10.1107/S0907444909042073 (2010). [PubMed: 20057044]
76. Schrödinger L The PyMOL Molecular Graphics System v.2.3. (2019).
77. Jo S, Kim T, Iyer VG & Im W CHARMM-GUI: a web-based graphical user interface for CHARMM. J Comput Chem 29, 1859–1865, doi:10.1002/jcc.20945 (2008). [PubMed: 18351591]
78. Quick M & Javitch JA Monitoring the function of membrane transport proteins in detergent-solubilized form. P Natl Acad Sci USA 104, 3603–3608, doi:10.1073/pnas.0609573104 (2007).

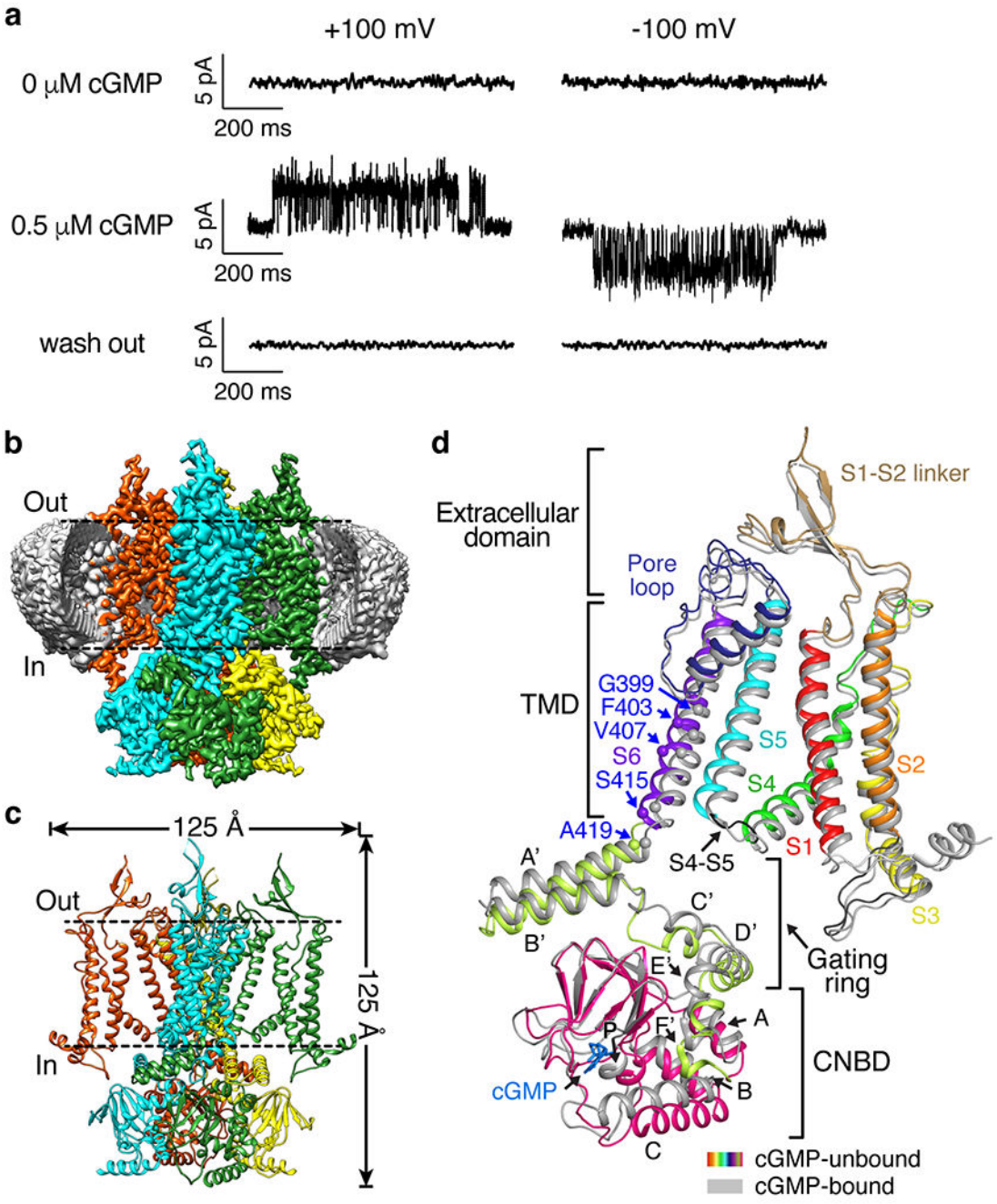

Figure 1. Cryo-EM structures of TAX-4 in cGMP-unbound and -bound states.

a, Single-channel currents of TAX-4 reconstituted in giant unilamellar vesicles. cGMP-induced currents were observed in 5/5 recordings. No basal activity was observed between −100 and +100 mV in any recordings. **b**, Cryo-EM density map of cGMP-unbound TAX-4 reconstituted in lipid nanodiscs (gray). **c**, cGMP-unbound structure, viewed parallel to the membrane. **d**, Superposition of cGMP-unbound and -bound protomer structures, viewed parallel to the membrane. S1-S6, pore-loop, C-linker and CNBD are illustrated in different colors. The α-carbon positions of five key amino acids are indicated.

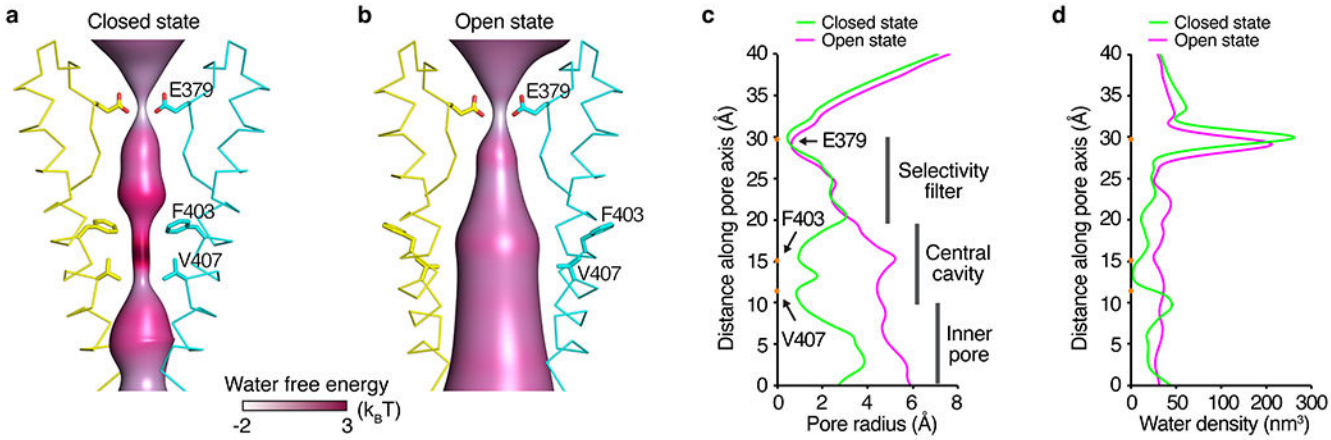

Figure 2. The ion permeation pathway of TAX-4 in closed and open states.

a,b, Water-accessible pathways in the closed (**a**) and open (**b**) states, generated with the CHAP program and color coded according to the water free energy. **c**, Pore-size profile of the indicated structures. The origin of the pore axis is set at the cytoplasmic end of S6. **d**, Water density profile.

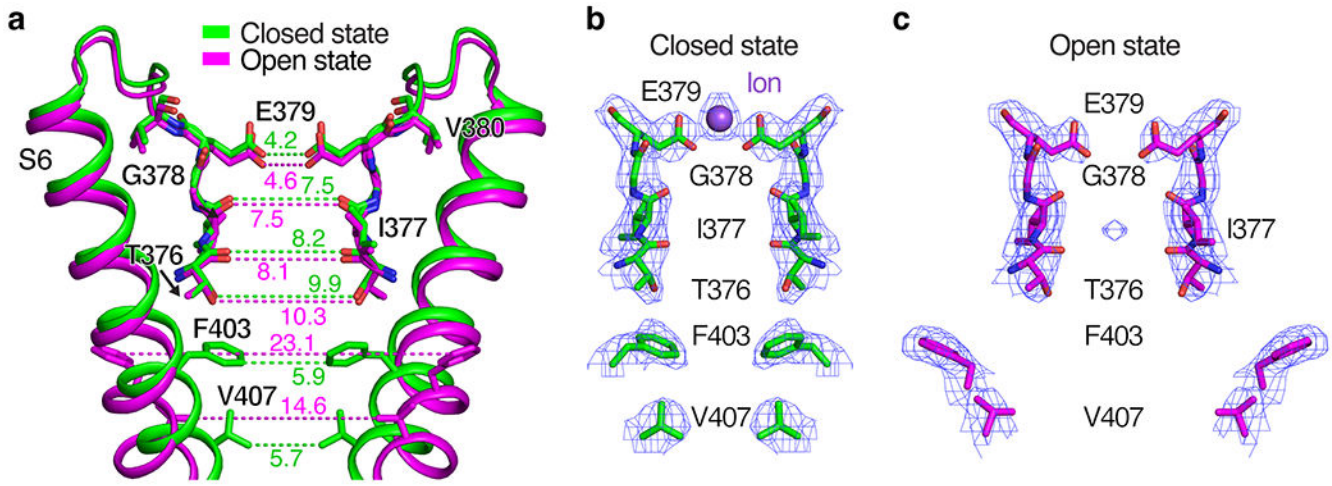

Figure 3. Comparison of the selectivity filter and central cavity in the closed and open states.

a, Comparison of SF and central cavity in closed and open states. Distances between the atoms are measured as the center-to-center distance of two diagonally opposed atoms. **b,c**, Close-up of the shown SF and central cavity residues in the closed (**b**) and open (**c**) states. Cryo-EM density maps (mesh) are contoured to 5σ. Purple sphere in (**b**) represents a presumed cation.

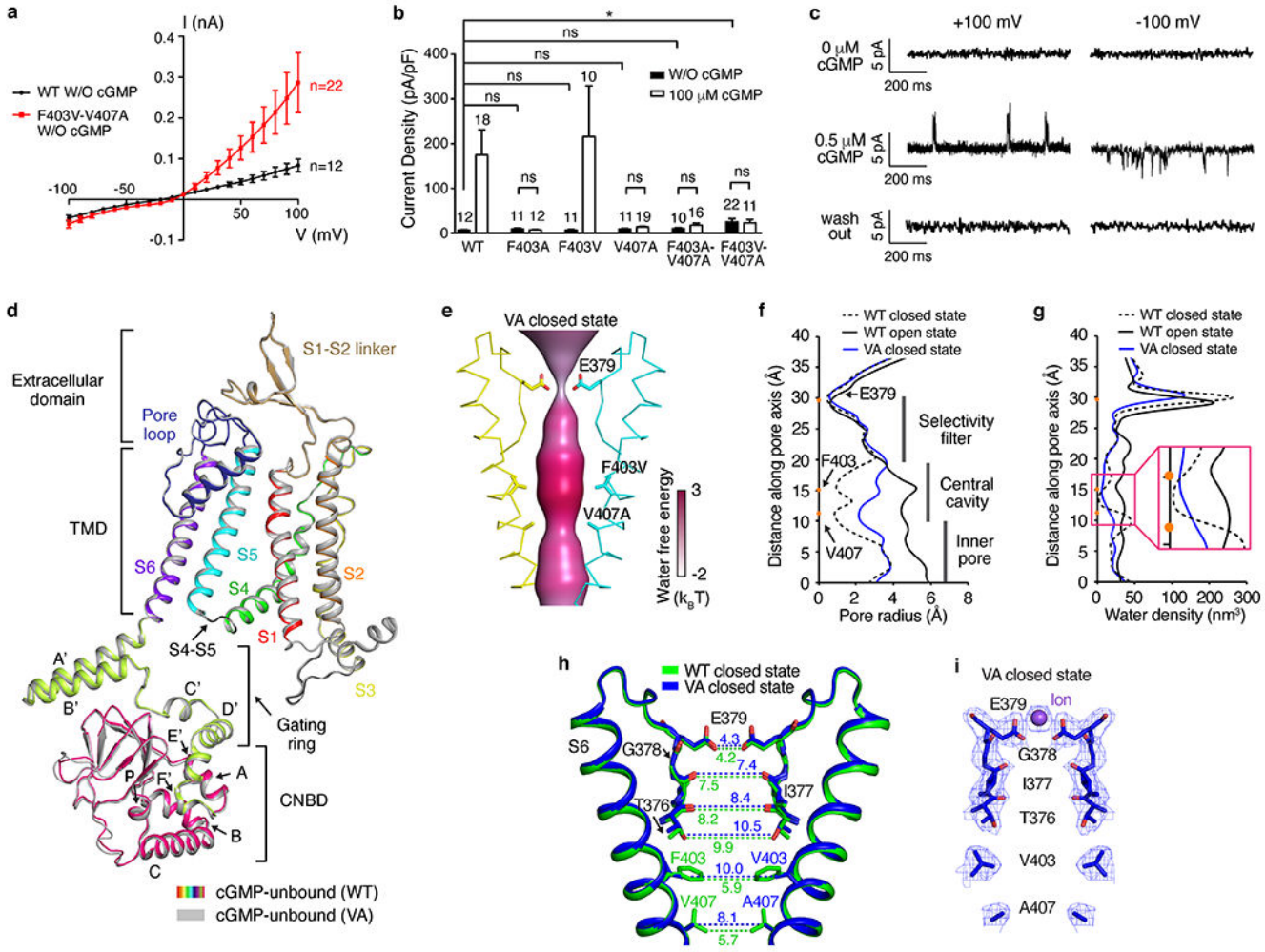

Figure 4. Functional, structural and computational analyses of F403V-V407A mutant TAX-4.

a, Averaged current-voltage relationships of whole-cell basal currents recorded in randomized and blind experiments from HEK 293T cells expressing F403V-V407A channels. The recording pipette contained no cGMP. n=number of independent measures. Error bars represent S.E.M. Original data are available as source data. **b**, Bar graphs summarizing whole-cell currents recorded at +100 mV from HEK 293T cells expressing WT and the indicated mutant channels, without or with 100 μM cGMP (to ensure maximum activation) in the recording pipette. Number of measurements is indicated for each condition. Error bars represent S.E.M. ns: no statistical difference. * $p<0.05$. Original data, error bar values, and statistical significance levels are available as source data. **c**, Single-channel currents of F403V-V407A mutant TAX-4 reconstituted in giant unilamellar vesicles. cGMP-induced currents were observed in 2/20 recordings. No basal activity was observed between −100 and +100 mV in any recordings. **d**, Superposition of WT and F403V-V407A (i.e., VA) cGMP-unbound protomer structures, viewed parallel to the membrane. **e**, Water-accessible pathways in the VA closed state, generated with the CHAP program and color coded according to the water free energy. **f,g**, Pore-size (**f**) and water density (**g**) of the VA closed state. Data for WT closed and open states were reproduced for comparison. The

origin of the pore axis is set at the cytoplasmic end of S6. Inset in (**g**) shows an enlargement of the indicated region. **h**, Comparison of SF and central cavity in WT and VA closed states. Distances between the atoms are measured as the center-to-center distance of two diagonally opposed atoms. **i**, Close-up of the shown SF and central cavity residues in the VA closed state. Cryo-EM density maps (mesh) are contoured to 5σ. Purple sphere represents a presumed cation.

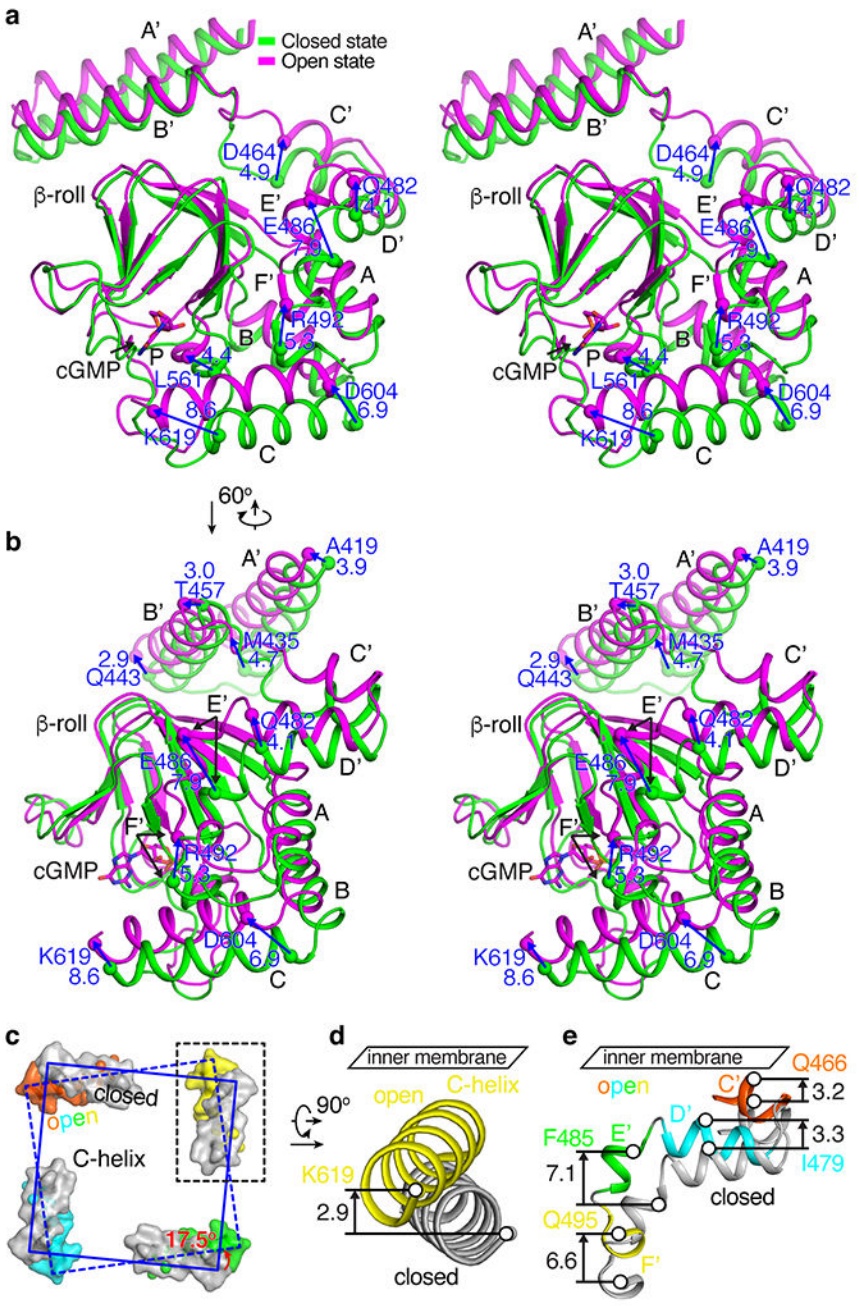

Figure 5. cGMP binding-induced conformational changes in the CNBD and C-linker.

a,b, Comparison of the CNBD and C-linker structures in closed and open states in stereo view. Blue arrows and numbers indicate cGMP-induced movements (in Å) of selected atoms in the two structures. **c**, Bottom-up view of rotation of C-helix in the CNBD upon cGMP-binding. **d**, Sideview of vertical movement of C-helix upon cGMP-binding. **e**, Sideview of vertical movement of helices C'D'E'F' in the C-linker upon cGMP-binding.

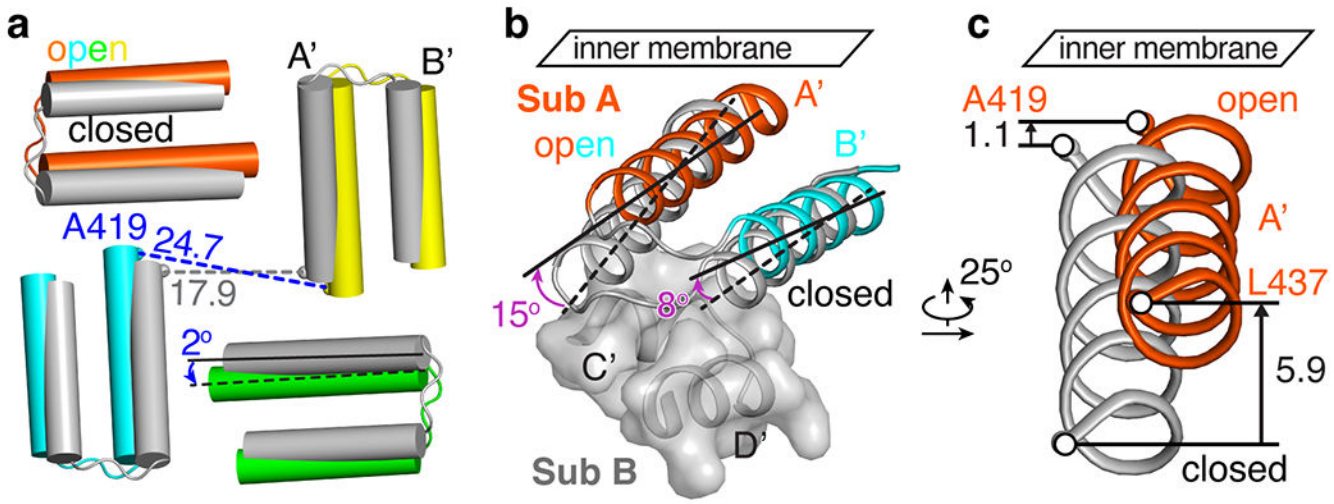

Figure 6. cGMP binding-induced conformational changes in the gating ring.

a, Bottom-up view of rotation and expansion of helices A'B' in the gating ring upon cGMP-binding. **b**, Sideview of upward tilting of helices A'B' upon cGMP-binding. **c**, Sideview of vertical movement of helix A' upon cGMP-binding.

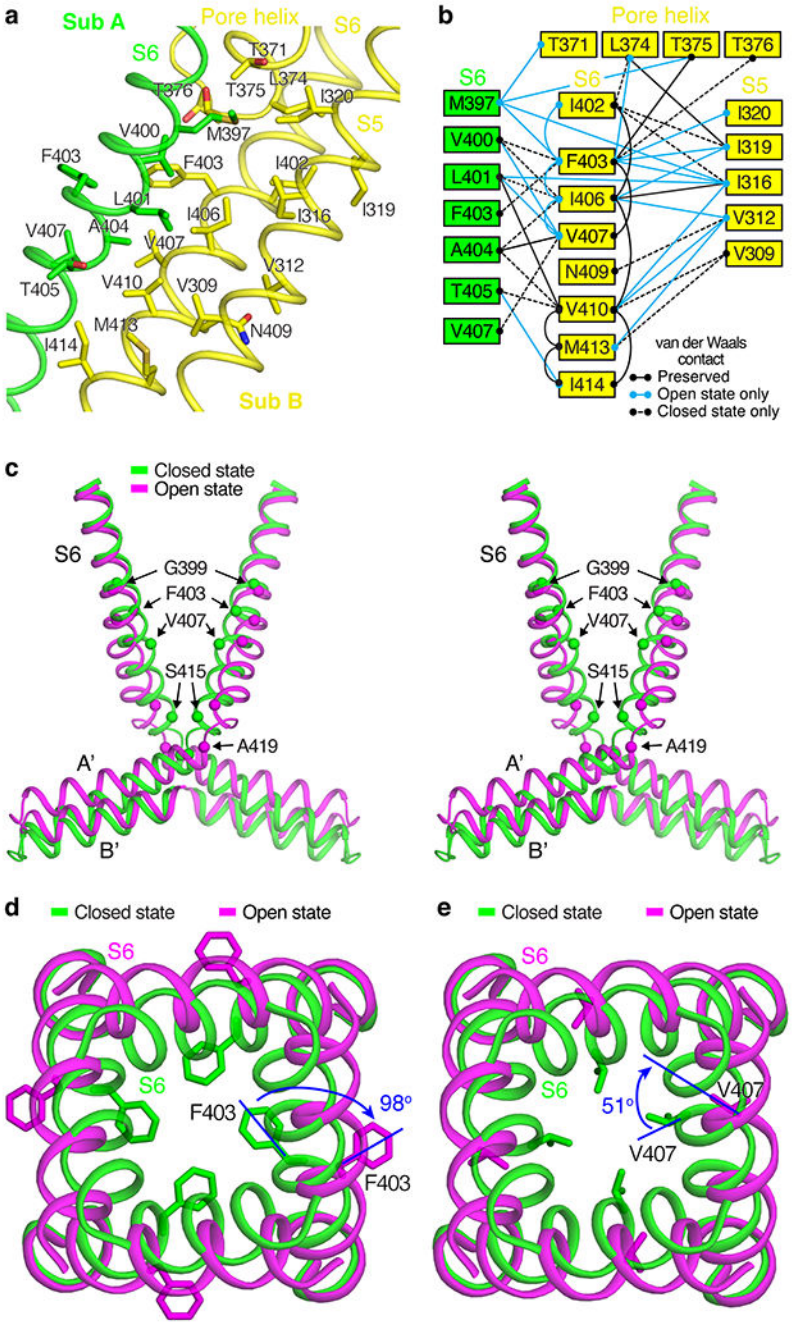

Figure 7. S6 interactions and cGMP binding-induced conformational changes in S6.

a, Interactions between S6 and S5, pore-helix and S6 of an adjacent subunit in the closed state. **b**, Diagram of specific interactions between S6 and S5, pore-helix and S6 of an adjacent subunit in closed and open states. **c**, Comparison of S6 and helices A'B' in closed and open states in stereo view. The α-carbon positions of five key amino acids are indicated. **d**,**e**, Comparison of S6 (viewed from the intracellular side) in closed and open states, highlighting the rotation of F403 (**d**) and V407 (**e**).

Table 1.

Cryo-EM data collection, refinement and validation statistics

	cGMP-unbound WT (EMD-21649, PDB 6WEJ)	cGMP-bound WT (EMD-21650, PDB 6WEK)	cGMP-unbound F403V/V407A (EMD-21651, PDB 6WEL)
Data collection and processing			
Magnification	22,500	22,500	130,000
Voltage (kV)	300	300	300
Electron exposure (e^{-}/Å^2)	66.03	66.03	56.45
Defocus range (μm)	−1.5 to −3.0	−1.5 to −3.0	−0.9 to −2.6
Pixel size (Å)	1.07	1.07	1.06
Symmetry imposed	*C4*	*C4*	*C4*
Initial particle images (no.)	801,931	617,269	1,877,870
Final particle images (no.)	163,525	128,685	445,131
Map resolution (Å)	2.6	2.7	2.5
FSC threshold	0.143	0.143	0.143
Map resolution range (Å)	2.4 to 3.0	2.4 to 3.0	2.4 to 3.0
Refinement			
Initial model used	PDB 5H3O	PDB 5H3O	PDB 5H3O
Model resolution (Å)	2.7	2.8	2.6
FSC threshold	0.5	0.5	0.5
Map sharpening *B* factor (Å^2)	−117.3	−112.5	−93.9
Model composition			
Non-hydrogen atoms	17,665	17,616	17,725
Protein residues	2,052	2,048	2,052
Ligands (cGMP/lipids/Na^+)	0/32/1	4/28/0	0/36/1
B factors (Å^2)			
Protein	79.28	72.23	80.84
Ligand	61.08	63.50	65.75
R.m.s. deviations			
Bond lengths (Å)	0.013	0.015	0.011
Bond angles (°)	1.016	1.031	0.789
Validation			
MolProbity score	2.11	2.38	2.08
Clashscore	8.77	10.08	8.22
Poor rotamers (%)	2.80	4.95	3.02
Ramachandran plot			
Favored (%)	95.68	95.23	96.07
Allowed (%)	4.32	4.77	3.93
Disallowed (%)	0	0	0